Final Technical Report

Project Title:	Dynamic Simulation over Long Time Periods with 100% Solar Generation
Project Period:	10/1/14-11/30/15
Submission Date:	1/19/16
Recipient:	Sandia National Laboratories
Address:	1515 Eubank SE Albuquerque, NM 87123
Website:	www.sandia.gov
Award Number:	Agreement No. 29095
Project Team:	Dr. Juan Sanchez-Gasca Dr. Matt Donnelly Ricky Concepcion
Principal Investigators:	Dr. Abraham Ellis Phone: (505) 844-7717 Email: aellis@sandia.gov Ryan Elliott Phone: (505) 844-8663 Email: rtellio@sandia.gov
Business Contact:	Shannon Boynton Phone: (505) 284-2631 Email: sboynto@sandia.gov
HQ Tech Manager:	Guohui Yuan, Ph.D.
HQ Project Officer:	Christine Bing

Acknowledgment

This research was supported by the U.S. Department of Energy, SunShot Initiative, under Agreement No. 29095. Sandia National Laboratories is a multi-program laboratory managed and operated by Sandia Corporation, a wholly owned subsidiary of Lockheed Martin Corporation, for the U.S. Department of Energy's National Nuclear Security Administration under contract DE-AC04-94AL85000.

SAND Number: SAND2015-11084 R

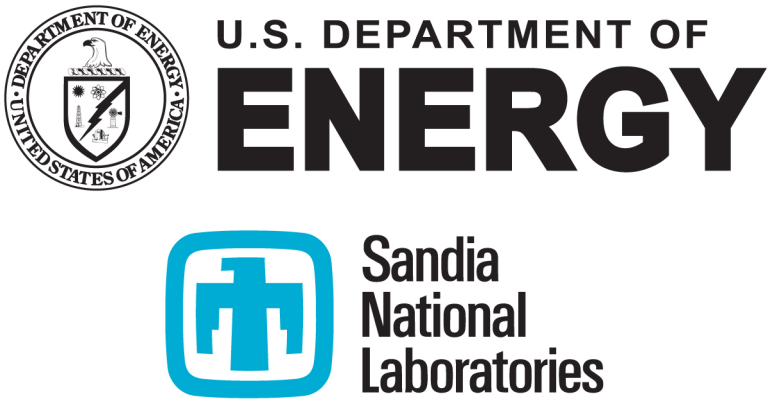

Executive Summary

This year-long project, supported by the SunShot Initiative, aimed to identify the path forward for dynamic simulation tools to accommodate these needs by characterizing the properties of power systems (with high PV penetration), analyzing how these properties affect dynamic simulation software, and offering solutions for potential problems. It supports the goal of enabling 100s of GW of solar power by seeking to improve dynamic simulation capabilities, especially for systems with significant amounts of photovoltaic power. With improved modeling and simulation capabilities, grid behavior for high penetration scenarios could be more easily understood, resulting in more efficient operation and increased readiness for transient events. The studies we conducted were performed using freely available Power Systems Toolbox in MATLAB including cases and models such as the miniWECC.

We focused on improving the feasibility of extended-term dynamic simulations of power systems with very high PV penetration primarily from the perspective of numerical integration. Extended-term dynamic simulations are simulations of the power system for durations beyond the minute regime into several minutes and hours. Such simulation lengths are relevant in general as they allow the incorporation of slower system dynamics that are typically neglected for sub-minute simulations but are particular important for high penetration of PV as the dynamics relevant to PV, such as solar irradiance, change on an hour timescale. Therefore, interaction with other similarly slow dynamics needs to be considered when simulating such scenarios in order to have reliable fidelity.

We saw that moving into the extended-term regime presented issues such as increased computational burden and data storage use and proposed modifying how simulation software performs numerical integration in order to address these concerns. Since some of the most commonly used power system simulation software make use of the explicit second order Adams-Bashforth (AB-2) integration method, we investigated other explicit integration methods due to their relative ease of implementation.

Since numerical stability is a primary concern for numerical integration, we analyzed the dynamic stability properties of power systems with increased PV penetration. Small signal analysis enables us to identify the system description from an eigenvalue perspective, which is necessary for selecting an appropriate numerical integrator for stability reasons. We identified how different power system dynamic models affect system modes and what role they play in selecting an integrator. An initial hypothesis was that high penetrations of PV would increase system stiffness, which would require changes to the numerical integrator in order to accommodate the increased range of system dynamics. Based on our investigations, we found that while increased PV penetration does have an effect on system dynamic behavior, it is rarely a primary factor in stressing the selection of an integrator. We found that the presence of certain components, such as induction motor loads, is most often the driving force in integrator and step size selection. Although increases in PV penetration tended to cause system eigenvalues to drift left in the complex plane, potentially increasing system stiffness, we found that the system eigenvalues that defined system stiffness tended to remain static with respect to PV penetration. The main caveat of these studies is that these observations are based on the particular cases and dynamic models that we were working with. Based on preliminary results from analysis done in GE's PSLF software, the inclusion of different controls and dynamic models will cause results to vary.

We found that the fourth order Crane-Klopfenstein (CK-4) predictor-corrector scheme to be a viable numerical integrator because its region of absolute stability shape encompasses the entirety of typical power system eigenvalues even at increased step sizes. This potential increase in step size can produce a lot of

computational and storage savings for extended-term simulations. On the other hand, in terms of numerical stability, we found that this scheme is incompatible with high frequency, fast decaying modes associated with induction motor loads. In such cases, we found that Heun's method is similarly accommodating for system eigenvalues at a given step size and is a safe alternative when the system's dynamic characteristics are unknown or problematic for CK-4.

As a different approach to addressing the problem of extended-term simulations for high PV penetration scenarios, we performed time domain simulations with different PV penetration scenarios in order to understand how PV penetration affects system behavior. We studied two systems, the Kline-Rogers-Kundur (KRK) and miniWECC systems, using eigenvalue analysis and time domain simulations. We identified and verified the dominant modes from eigenvalue analysis using spectral estimation techniques on transient simulation results at increasing PV penetration levels. We found that while there is no definitive trend of mode damping with increased PV penetration, system eigenvalues were likely to drift left in the s-plane, which may become a factor in numerical stability. Additionally, we observed issues associated with reduced system inertia through generation drop simulations, such as lower frequency nadirs, slower recovery, and lower settling frequency.

We identified a need to improve system dynamics modeling, especially for slower and faster dynamics (such as automatic generation control (AGC) and the phase-locked loop (PLL), respectively) and proposed a simulation framework to improve our capabilities to model high PV penetration scenarios.

Overall, this project was successful in identifying a path forward for making extended-term dynamic simulations for high PV penetration scenarios viable. We highlighted some candidate numerical integrators that would be more suitable for these types of simulations. We also identified some gaps in modeling that need to be addressed in order to improve simulation fidelity. While questions remain on how to address these limitations, we have provided directions that future research should take on to improve power system simulation capabilities.

Contents

1 Background

In the quest for a clean and sustainable future, there exists a large push towards incorporating substantial amounts of renewable energy sources such as photovoltaic (PV) generation. The uncontrolled intermittent availability of renewable energy sources makes integration of such devices into today's grid very challenging. Technical issues include energy and power balancing, voltage regulation and stability, frequency regulation, transient stability, and small-signal stability. Another challenge is that the characteristics of a grid with high PV penetration, e.g. 100% of load, will have dynamics significantly different from the grid of today. Currently, transient simulations capture the electro-mechanical response of the grid to various disturbances. A grid dominated by inertia-less generation (e.g. renewables with inverters) will potentially be more responsive to disturbances.

The topic of extended-term time-domain simulation for electric power systems is beginning to garner increasing attention in the literature. In [1], the authors proposed an integration method called Hammer-Hollingsworth 4 (HH-4), which is a special case of the implicit fourth order Runge-Kutta method that is A-stable, possesses the same stability domain as the trapezoidal rule (2nd-order Adams-Moulton method), and has a higher order of accuracy than the trapezoidal rule [2].

A numerical method is said to be A-stable if all of its solutions to equations of the form:

$$\frac{\mathrm{d}}{\mathrm{d}t}y = ky, k \in \mathbb{C} \tag{1.1}$$

$$y(t) = Ae^{kt} \ \forall \ \mathrm{Re}(k) < 0 \tag{1.2}$$

decay to zero as $t \to \infty$ [3]. This means that for differential equations for which the true solution decays to zero as a function of time, the numerical solution also decays, rather than diverging. Equivalently, a method is A-stable if its region of stability contains all of the left half-plane [3]:

$$\text{Region of Stability} \supseteq \{h\lambda \in \mathbb{C} | \mathrm{Re}(h\lambda) < 0\} \tag{1.3}$$

where h represents the simulation step size and λ represents the continuous-time system eigenvalues.

Because the HH-4 method is implicit, the state update equations constitute a nonlinear system which must be solved iteratively. This makes the method much more computationally intensive than linear multistep methods and predictor-corrector schemes and dependent on the specific set of differential equations. Additionally, all fourth order Runge-Kutta methods including HH-4, require the calculation of the state derivatives to be performed four times per integration step. In contrast, a predictor-corrector scheme based on the trapezoidal rule requires the state derivatives to be calculated only twice. The region of stability of the trapezoidal rule is ideal because it includes all of the left half of the complex plane, and none of the right. However, the trapezoidal rule is also an implicit method, which makes it nontrivial to implement in software in addition to its computational challenges. The integration techniques collectively called predictor-corrector methods serve as a compromise in which the solution to an implicit method is approximated using purely explicit formulations [4].

At present, the standard commercial tools for performing time-domain simulation of large-scale power systems employ explicit, multistep numerical integration methods with a fixed step size. The integrator employed by PSLF and PSS/E, the second order Adams-Bashforth method (AB-2), has a region of stability that is a subset of the left half of the complex plane. This means that the currently employed numerical integration schemes have the potential to exhibit numerical instability for stable systems [5].

An ideal numerical integration scheme for dynamic simulation purposes would possess a larger region of stability and a higher order of accuracy than AB-2. An intelligently chosen predictor-corrector scheme

could satisfy both criteria. Since predictor-corrector schemes are explicit formulations, they cannot be A-stable like the trapezoidal rule [6]. However, they can possess a significantly larger region of stability than AB-2, allowing for larger simulation step sizes [7]. Using such larger step sizes means that fewer numerical integration iterations are required to simulate the same duration of time. As a result, fewer data need to be computed and stored, reducing the computational burden of performing the extended-term dynamic simulations which are necessary for analyzing the behavior of high PV penetration scenarios.

The practical implication of this is that the choice of step size for an explicit integration scheme will impact whether or not it exhibits numerical instability. However, numerical stability cannot be the only consideration for integrator selection. There is an inherent trade-off between numerical accuracy and computational workload when the step size of a simulation is modified; in general, simulations run faster at the expense of accuracy with larger step sizes. For explicit methods, the step size must be tuned appropriately such that the eigenvalues of the system reside within the region of stability. Therefore, it is essential to understand the eigenvalue topology of typical power system models, possibly with very high PV penetration, in order to make the best compromise on numerical integrator selection that makes extended-term simulations viable.

2 Project Objectives

The goal of this study was to develop a path forward for dynamic simulation tools that enable analysis of power system performance (with high PV penetration) for a period of minutes to hours. The uncontrolled intermittent availability of renewable energy sources makes integration of such devices into today's grid very challenging. This effort looked at the fundamental drivers, the algebraic and differential equations that model a grid with 100% PV generation, to identify the path forward for dynamic simulation tools that support high renewables as well as longer simulation times which are required to better characterize the impact of renewable variability on dynamic performance.

The general approach to accomplish this goal was as follows:

1. Identify the characteristics and requirements for large-scale simulation of a power grid with PV generation equal to 100% of load.
2. Identify appropriate numerical integration techniques.
3. Quantify the small signal stability and transient response of 100% PV scenarios using models studies to assess these numerical integration techniques. This was done using both small and large representative example systems.
4. Present results to stakeholders and vendors and incorporate feedback into research approach.

Early on, we determined that increasing PV generation levels to near 100% of load was problematic for simulation software and, realistically, would require significant changes to both how power systems are modeled and operated and how they are simulated. Therefore, our research focused on levels of PV generation where simulations could be performed without the implementation of additional controls.

In comparison with Agreement No. 29094 (Byrne-A), we used similar tools such as PST and its linearization routines as well as similar test cases. While both projects focused on systems with high levels of PV penetration, each project sought to support SunShot's goals in different ways. For this project, we used the aforementioned tools and test cases to study the small signal stability properties of

representative power systems to assess the requirements for supporting dynamic simulations as described in the project title. Therefore, there was no effort put into improving the systems from a stability perspective by considering different ways to increase PV penetration while maintaining stability through, e.g., controls design. This was the objective in Byrne-A. As a result, the systems in Byrne-A were able to achieve higher PV penetration levels. The control schemes developed in Byrne-A would help in reaching target levels of PV penetration but also potentially add new dynamics that may affect dynamic simulation requirements, i.e., through the addition of eigenvalues that may affect numerical stability. Nevertheless, while the approaches differed slightly in each of these two projects, the results of both time and frequency domain analyses corresponded closely.

This project helps support SunShot's goals of developing technologies to enable high penetrations of PV generation by improving the state of the art in power system simulation software. By improving the capabilities for realistically simulating high PV penetration scenarios, the understanding of grid behavior under such conditions can be improved so that large amounts of PV generation can be reliably and efficiently implemented.

3 Project Results and Discussion

3.1 Characteristics and Requirements for Large-Scale Simulations with High PV Penetrations

In stability studies, the dynamic behavior of a power system can be fully described by a set of algebraic equations that is a coupled to a system of differential equations [7]. The characteristics of the algebraic and differential equations required to accurately simulate systems with high PV penetrations stem from augmentations of traditional dynamic simulation formulations. The two basic sets of equations that constitute the simulation framework have the following form [8]:

$$\text{(differential)} \qquad f(x, v) = \frac{\mathrm{d}}{\mathrm{d}t}x \tag{3.1}$$

$$\text{(algebraic)} \qquad g(x, v) = Yv - i(x, v) = 0 \tag{3.2}$$

where:

$x \triangleq m \times 1$	vector of state variables
$\frac{\mathrm{d}}{\mathrm{d}t}x \triangleq m \times 1$	vector of state variable derivatives with respect to time
$v \triangleq n \times 1$	vector of complex bus voltages
$Y \triangleq n \times n$	network admittance matrix
$i \triangleq n \times 1$	vector of complex current injections at each bus

In practice, the vast majority of inverter-coupled renewable generation is supplied by voltage-source converters (VSCs) [9]. Voltage-source converters are high-bandwidth current regulators [9]. At a high level, the objective of inverter control schemes is to regulate current to maintain desired real and reactive power output levels. In the set of algebraic equations, the current injections from PV inverters are accounted for using the same physical description as constant current loads. For VSCs the real power "load" is negative,

indicating a net injection into the grid. In the equations below, the P_i and Q_i terms indicate the constant current components of the injection.

$$P = P_p + P_i|v| + P_y|v|^2 \tag{3.3}$$
$$Q = Q_p + Q_i|v| + Q_y|v|^2 \tag{3.4}$$

The algebraic and differential equations that describe the dynamic behavior of a power system are coupled together and must be solved at each time step. This coupling can be seen more clearly by expressing the two sets of equations in a slightly different way:

$$E\frac{\mathrm{d}}{\mathrm{d}t}y = w(y) \tag{3.5}$$

where:

$$y \triangleq \begin{bmatrix} x \\ v \end{bmatrix} \tag{3.6}$$
$$w \triangleq \begin{bmatrix} f \\ g \end{bmatrix} \tag{3.7}$$
$$E \triangleq \begin{bmatrix} I & 0 \\ 0 & 0 \end{bmatrix}, \quad I \triangleq m \times m \text{ identity matrix} \tag{3.8}$$

This yields a single set of equations, the total number of which is equal to the sum of the number of state variables plus the number of buses in the system.

3.1.1 Simulation software prototyping and modeling PV generation

After careful consideration, we selected Power Systems Toolbox (PST) for MATLAB as the simulation environment for this project [10]. This decision was based on project team members' existing experience with the software in addition to its long track record of providing value to the R&D community. PST was originally conceived by Dr. Joe Chow at Rensselaer Polytechnic Institute (RPI) and later upgraded and maintained by Dr. Graham Rogers at Cherry Tree Scientific Software. It was designed to enable scientists and engineers in the research community to perform power flow and dynamic analysis directly in MATLAB, without having to resort to commercial software tools that are both computationally and financially expensive. PST has the benefit of being open source, and completely modifiable. This means that the platform enables researchers to implement custom numerical integration algorithms, which is of course impossible in environments like PSLF and PSS/E.

Dr. Trudnowski at Montana Tech uses PST extensively for modal analysis of the Western Interconnection using a reduced order model of the system (the "miniWECC") [11]. This model was invaluable in this project as a relatively larger test case which could be validated against existing research using both the mini WECC and more complete representations of the Western Interconnection. Additionally, Dr. Trudnowski aided the project team by providing a modified version of PST that includes the ability to model arbitrary power or current injections into a bus. We used this utility to model PV generation as constant current injections [11]. This method of modeling PV has its limitations, especially due to the absence of controls present in generic models used for other studies; an example of this is demonstrated

using PSLF later in this section. However, this method of modeling PV empirically produces results that are expected of inertialess generation. This is demonstrated in time domain simulations in a later section.

We described increases in PV penetration by creating a parameter that we called the "solar fraction." This continuous, fraction-valued parameter is used to shift power generation from synchronous machine sources with inertia to inertialess sources modeled as current injections — our implementation of PV generation. In order to model the relative decrease in reactive power output by PV generation, we reduced the amount of reactive power produced by an aggregate of sources as solar fraction values increased. In this project, we used a 50% reduction. For example, suppose that representative plant A in a system model is slated to produce 7.00 p.u. active power and 1.61 p.u. reactive power when all of its constituent units are synchronous machines. If we declare that this system has 50% PV, then the machine representing synchronous generation at plant A will produce 3.50 p.u. active power and 0.805 p.u. reactive power. Meanwhile, the device representing PV generation at plant A will also produce 3.50 p.u. active power but only 0.4025 p.u. reactive power. Additionally, the mVA base of the machine at plant A is reduced by 50% to model the reduction of inertia as generation shifts to an inertialess source. In short, PV% throughout the analysis in this report refers to the solar fraction value used in each simulation; essentially, it is a parameter that relates to total system generation rather than system load.

Throughout this study, we analyze scenarios that are primarily characterized by PV%. As explained in the previous paragraph, this parameter describes how much generation has shifted towards the modeled PV generation and, correspondingly, how much system inertia has been reduced.

3.2 Background on Linear System Stability

Previously, we discussed the stability of a numerical method in the context of A-stability. While A-stability is a property of a numerical method, we would like to discuss numerical stability, which is a property of a specific numerical integrator for a particular dynamical system. Numerical stability, as used in this study, refers to a numerical integration scheme with a particular step size being stable in the same sense as A-stability for a particular system. In other words, if all solutions for a set of differential equations that decay to zero over time also decay to zero using a particular numerical integrator, then that integrator is numerically stable for that system. By extension, an integrator that is numerically stable for one system may not be numerically stable for another system because their eigenvalues may be different.

3.2.1 Region of absolute stability

This brings up the concept of regions of absolute stability. This property of a numerical integrator allows one to determine if the integrator is numerically stable for a specific system. If all of the eigenvalues of a system reside within the region of absolute stability for a numerical integrator, then the integrator is numerically stable. These regions are subsets of the complex eigenvalue plane and can be computed in a straightforward manner. Refer to the following example.

Example: Region of absolute stability for explicit Forward Euler method The Forward Euler method is defined using the recurrence relation:

$$y_{n+1} = y_n + h\frac{\mathrm{d}}{\mathrm{d}t}y_n \tag{3.9}$$

where $\frac{\mathrm{d}}{\mathrm{d}t}y_n = \lambda y$. Now let $w^k = y_{n+k}$ (similar to a z-transform) and let $\bar{h} = h\lambda$. Applying these transformations and substitutions to the recurrence relation yields:

$$w = 1 + h\lambda(1) = 1 + \bar{h} \tag{3.10}$$

The resulting expression is called the stability function, a function of $\bar{h}$. The region of absolute stability is the region of the $\bar{h}$-plane for which the magnitude of the roots of the stability function is less than unity. For this example, the region of absolute stability is:

$$\text{Region of Stability} = \{\bar{h} : |1 + \bar{h}| < 1\} \tag{3.11}$$

This defines a disk in the $\bar{h}$-plane centered at -1 with a radius of unity.

It is important to note that the region as calculated above is defined in the $\bar{h}$-plane. This means that in order to map it to the complex eigenvalue plane, it must be scaled by $1/h$. Hence, the region of absolute stability size is inversely proportional to simulation step size. This implies that larger step sizes may result in numerical instability; this is also why system stiffness can roughly approximate how small the step size for a simulation needs to be.

To demonstrate the effect of numerical stability on dynamic simulations, we created a test platform in MATLAB. We used a system described by a simple second order differential equation with a complex eigenvalue pair $s = \sigma \pm j\omega$ and simulated the step response of the system. Since the analytical solution is known, we can compare it to the simulated response to illustrate how numerical stability affects simulation quality.

Example: 2nd order ODE

Case 1: System eigenvalues at $s = -1 \pm j2$ The system eigenvalues are well within the region of absolute stability for the integrator. The simulated response slightly deviates from the analytical solution but converges correctly.

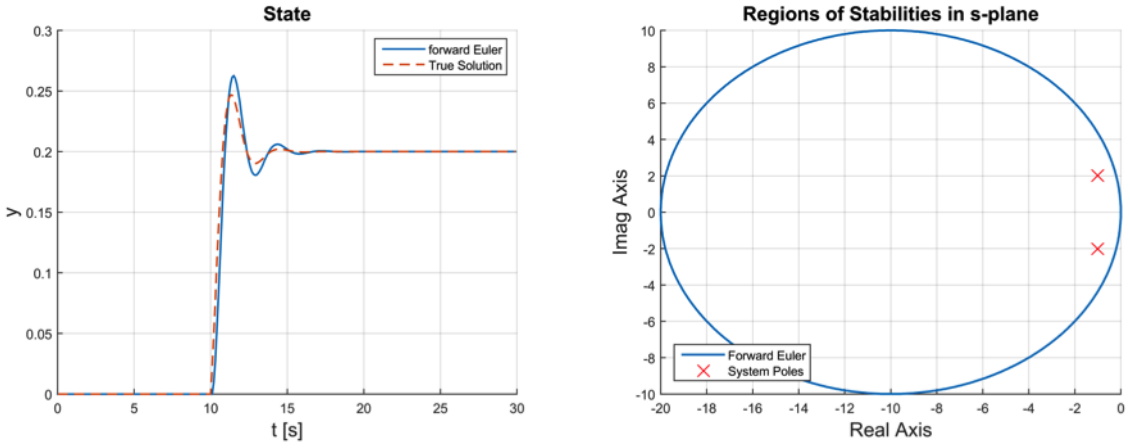

Figure 1: This integrator is numerically stable for this system.

Case 2: System eigenvalues at $s = -0.5 \pm j2$ The system eigenvalues are encroaching upon the region boundary from within. The simulated response is stable but not accurate — it exhibits numerical oscillations.

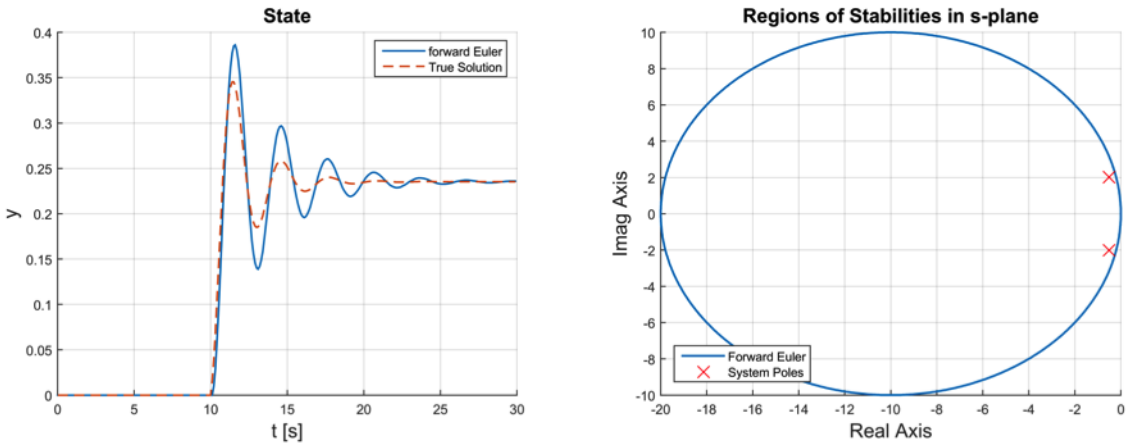

Figure 2: This integrator is numerically stable for this system but suffers from numerical oscillations.

Case 3: System eigenvalues at $s = -0.1 \pm j2$ The system eigenvalues are outside the region of absolute stability. The simulated response is unstable and inaccurate — the analytical solution is stable but the simulated response diverges. The simulation is not only inaccurate but qualitatively incorrect.

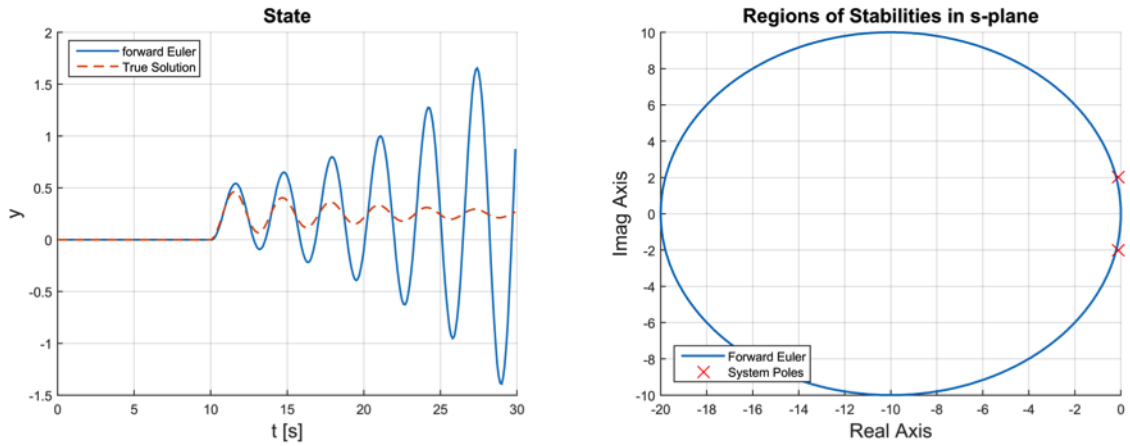

Figure 3: This integrator is numerically unstable..

The takeaway here is that for a given numerical method, it is essential that the numerical integrator be stable. Furthermore, depending on preference, it is important to keep in mind that numerical oscillations will occur if system eigenvalues are stable but near the boundary of the region of absolute stability.

In this study, we sought to propose suitable integration schemes for dynamic simulation over long time periods. One method of increasing extended-term simulation viability is to increase the step size of the integrator. As we have demonstrated, we are limited in this regard by numerical stability. For

implicit methods, numerical stability is not much of a concern as A-stability is a possibility whereas it is not for explicit methods. However, implicit methods tend to be relatively difficult to implement and computationally expensive. For improved accuracy, we would also like to consider higher order numerical methods but likewise they come at the cost of increased computation and memory needs.

3.2.2 Stiffness overview

One of the hypotheses of this study was that system stiffness would increase with PV penetration. System stiffness is a property of the set of differential equations that describe the dynamics of the system. To measure system stiffness, we used the stiffness ratio:

$$\text{stiffness ratio} = \frac{\max|\text{Re}(\lambda)|}{\min|\text{Re}(\lambda)|} \tag{3.12}$$

This property of a system of differential equations roughly describes the range of dynamics present in the system; a large stiffness ratio implies that there are modes with very fast decay rates, very slow decay rates, or a combination of both. Intuitively, this represents a type of difficulty in integrating the associated differential equations; both fast and slow dynamics need to be accounted for. However, the simplicity of this quantity implies that it may not be sufficient to wholly describe a system's characteristics with respect to numerical integration.

In order to analyze the stiffness of power systems, we used PST's linearization capabilities. Tools included with PST for small signal stability studies enable users to estimate properties of power system test cases such as system eigenvalues and associated left and right eigenvectors. Throughout this report, we show what we call "eigenvalue sweep maps." These are similar to root locus diagrams where the parameter that is swept is the PV%. Starting at the nominal case, which is the scenario where there is no PV generation, we estimated the system eigenvalues using the linearization capabilities and plotted them in the complex plane in blue. In increments of 5%, we increased the PV% and estimated the system eigenvalues and plotted them in green. This process continued until reaching some pre-determined bound on PV%; the eigenvalues corresponding to this case are plotted in black. The purpose of these graphics is to illustrate the trajectory of system eigenvalues as a function of PV penetration.

In the next section, we study two representative power system models and examine how system stiffness impacts numerical integrator selection.

3.3 Stiffness Analysis

In this section, we examine the system eigenvalues and stiffness of a small, 13-bus test case, the Kline-Rogers-Kundur (KRK) system as well as a larger test case, the miniWECC.

3.3.1 Kline-Rogers-Kundur (KRK) system

This test system [12] was created to study interarea and local modes using a small, simple, but realistic setup. It was included with PST in a variety of flavors. We modified a version of it that was loaded with subtransient machine models, IEEE type DC1 excitation systems, and simplified turbine/governor models. We added PV generation to this system that varied depending on the study.

In the following eigenvalue sweep diagrams, the system eigenvalues are plotted in the complex s-plane. As we will observe, this arrangement of system eigenvalues seems to be prototypical for the test cases encountered thus far. Typically, the relatively higher frequency eigenvalue pairs in the 0.8-1.6 Hz range

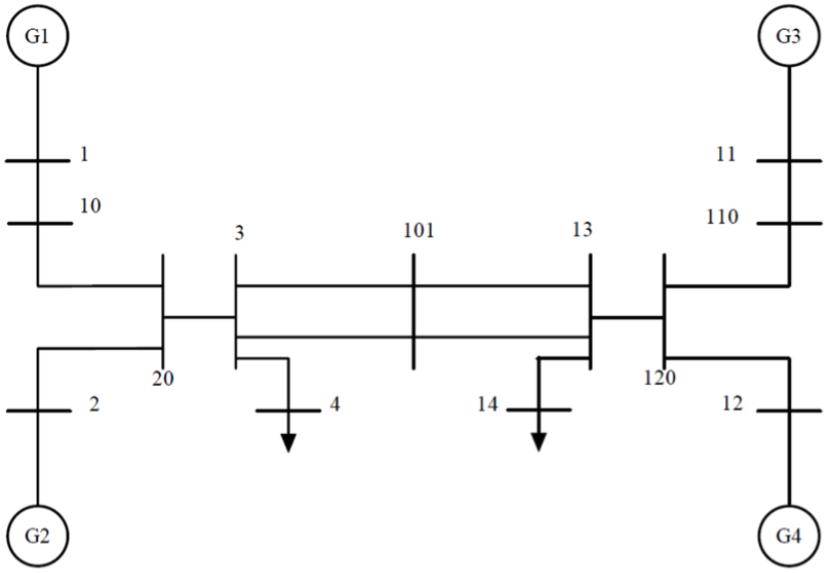

Figure 4: The Kline-Rogers-Kundur system one line diagram.

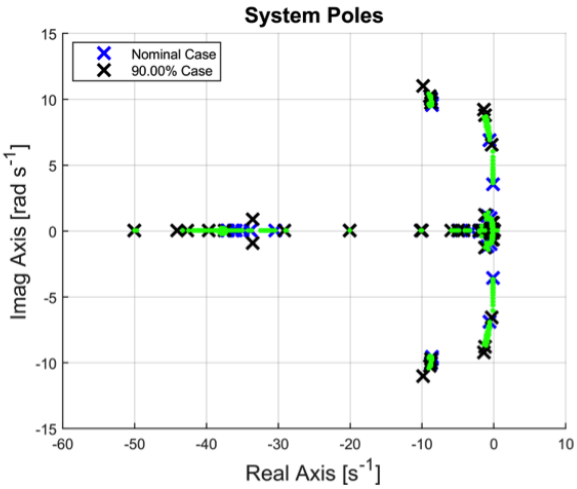

Figure 5: System eigenvalue sweep map.

have larger time constants and tend to aggregate near the $j\omega$-axis. The largest magnitude eigenvalues in most cases tend to be purely real. Upon further investigation, the location of the largest magnitude eigenvalues is directly governed by the smallest time constant in the system, which tends to be part of the exciter dynamics.

It was hypothesized that increased solar penetration levels would increase system stiffness. As we have shown in Figure 7, this is definitively not the case. Empirically, we cannot conclude that an increase in solar penetration levels definitely increases the stiffness of the system. In this system, we observe the opposite: increasing solar penetration decreases system stiffness. This can be explained by the fact that, since the numerator of the stiffness ratio tends to be invariant with respect to solar penetration, the stiffness ratio

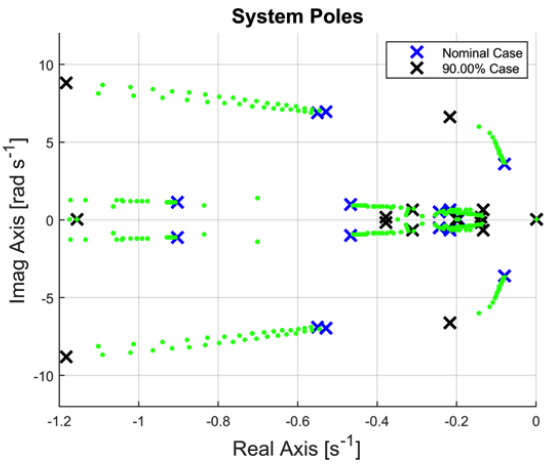

Figure 6: Zoom-in of system eigenvalue sweep map in Figure 5, focusing on lightly damped modess.

is entirely governed by (and highly sensitive to) changes in $\min |\mathrm{Re}(\lambda)|$. Anecdotally, we can see massive orders of magnitude differences in stiffness ratio across solar penetration levels due to this sensitivity and eigenvalues sweeping across and around the s-plane origin. In order to mitigate large variations in stiffness ratio that may obscure trends due to hypersensitivity, we only considered eigenvalues with real parts no larger than some threshold when computing $\min |\mathrm{Re}(\lambda)|$.

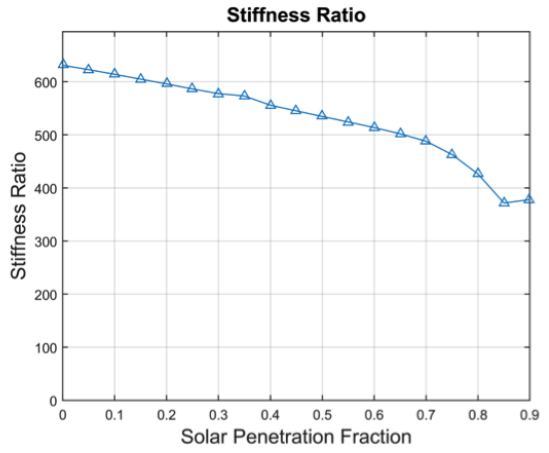

Figure 7: Stiffness ratio against PV%.

We used PST's linearization capabilities to try to identify the local and interarea modes of the system. Compass plots were selected to aid in visualizing mode shapes and identifying the types of modes present in the system. These plots were generated by determining the right eigenvector (mode shape) of the associated with the eigenvalue indicated in the title of each plot. Each entry in these complex-valued vectors correspond to a state in the system; these complex numbers are translated to vectors in the complex plane for the compass plots. Mode shape eigenvectors were normalized such that the largest magnitude component in each eigenvector served as the reference $1 + j0$. Selected state variables, typically machine speeds, were plotted to clearly illustrate state relationships.

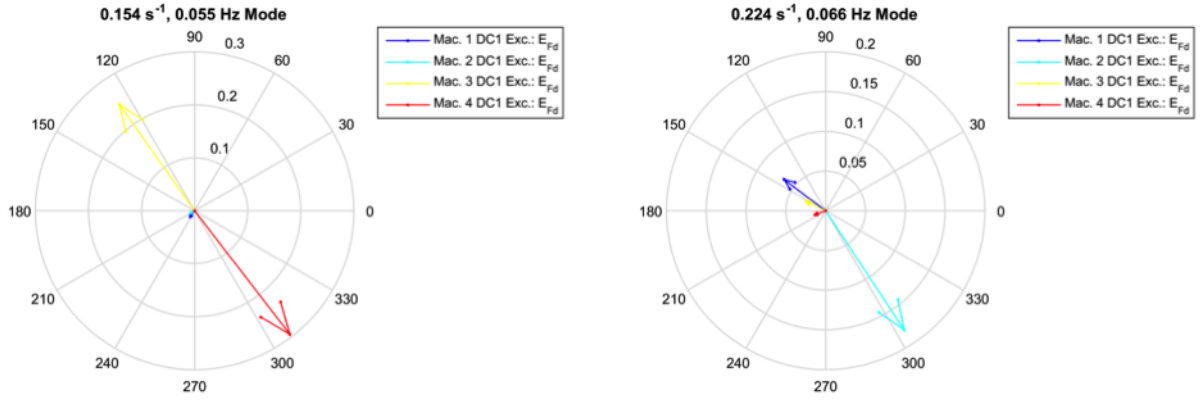

Figure 8: Compass plots of local modes of the KRK system base case. (left: area 1, right: area 2)

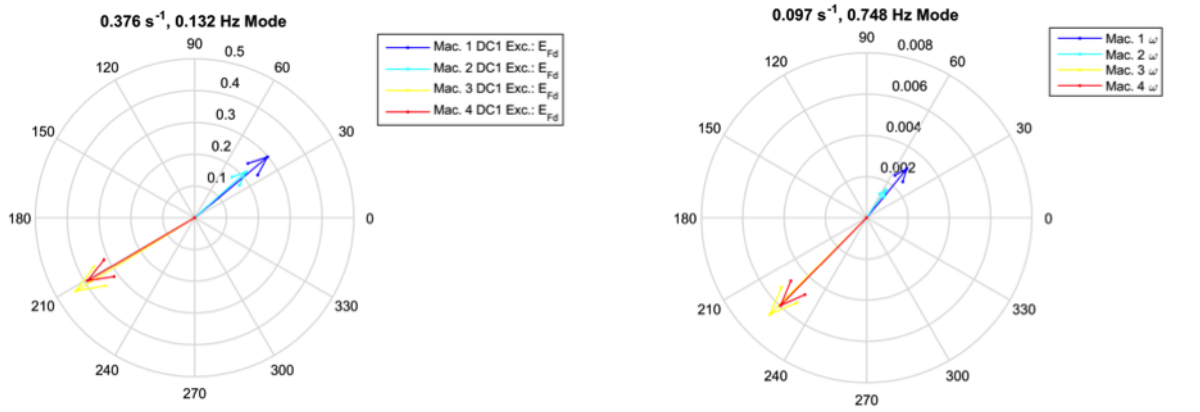

Figure 9: Compass plots of interarea modes of the KRK system base case.

In order to characterize the effect of increased PV% on system modes, we tracked the trajectory of the interarea mode as the solar fraction increased. We computed the damping ratio, ξ, based on the interarea mode eigenvalue at four different solar fraction values. The results are summarized in Table 1. We observe that the damping ratio decreases very slightly with increased PV penetration; however, it is difficult to generalize this trend across all systems.

Table 1: Damping ratio for different modes in KRK system.

Mode	α [$\mathbf{s}^{(-1)}$]	**f [Hz]**	ξ [%]
Interarea (0%)	0.07928	0.5710	2.21%
Interarea (25%)	0.08400	0.6150	2.17%
Interarea (50%)	0.09358	0.7044	2.11%
Interarea (60%)	0.09700	0.7480	2.06%

Analysis in PSLF To provide another perspective on our analysis, we recreated the KRK system in PSLF. The intent was to recreate the KRK system with as similar operating conditions and model parameters as the PST case as possible. This comes with the caveat that the dynamic models available in each software platform differ. For example, instead of using the older, IEEE type DC1 exciter models, we used AC4 excitation systems. Most notably, instead of using the simple model for PV generation that we used in PST, we used more sophisticated models for photovoltaic plants that include, for instance, electrical controllers.

Analogously to what was done in the PST studies, we performed a root locus sweep of active power generation. The base case has all power generation in the system coming from synchronous machines. In 20 increments of 35 MW, active power generation is shifted to photovoltaic power plants while reactive power generation is maintained by the synchronous machines. The resulting system eigenvalue map is shown in Figure 10.

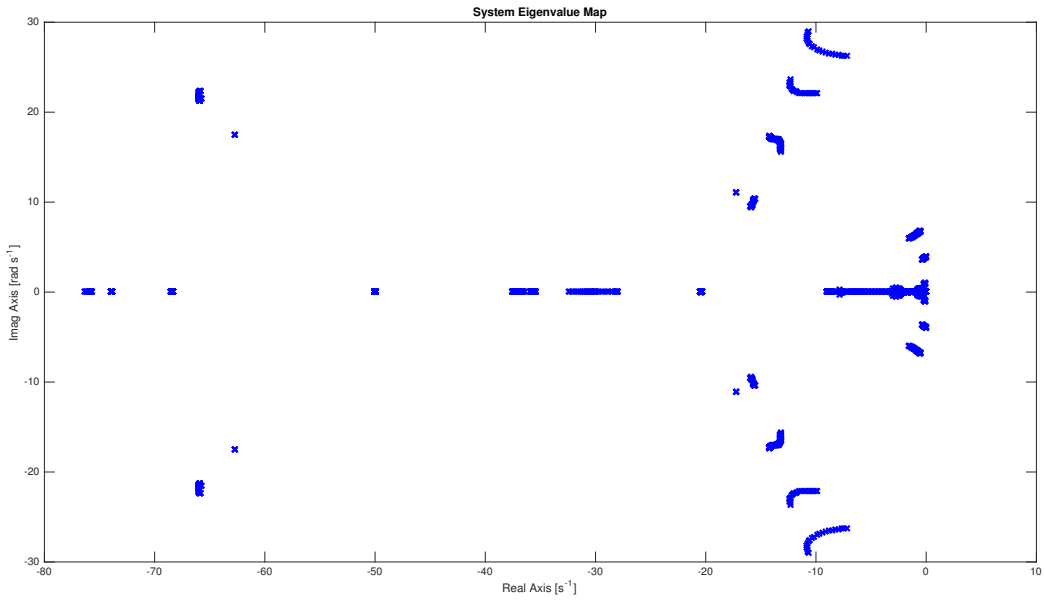

Figure 10: PV% sweep of KRK system equivalent in PSLF. The results shown differ from the analysis in PST primarily due to the usage of different dynamic models.

It is important to note that these results are preliminary as the photovoltaic power plants have not particularly been used to model these types of systems. Focusing on the interarea and local modes, we observe that these modes exhibit an increase in damping as the power generation is shifted to the PV power plants. Contrary to the analysis in PST, these modes primarily increase in damping rather than in frequency; this results in different trends of damping ratio. Additionally, even in the nominal base case, we observe that there are higher frequency modes present in the PSLF system compared to the PST system. In particular, the presence of higher frequency with fast decay rates in the PSLF case could prove to be problematic for dynamic simulations with increased step sizes. Nevertheless, we can attribute the appearance of these different modes in the PSLF study to the different dynamic models used, e.g., the electrical controllers. As these models have not been typically used for these types of studies, it remains to be seen if the general trends correspond to what was observed in the PST analysis.

3.3.2 miniWECC system

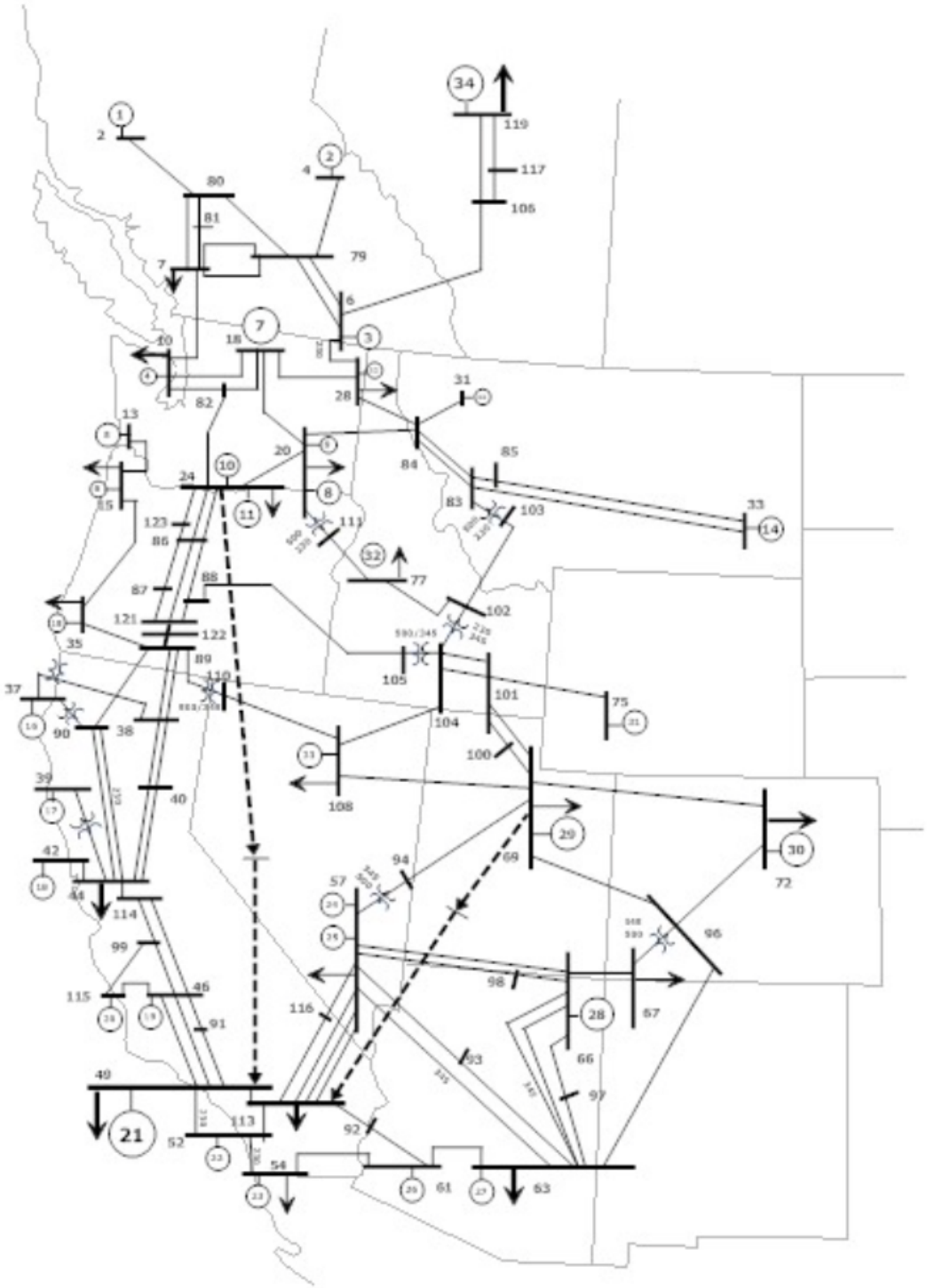

Figure 11: The miniWECC system one line diagram, taken from [13].

The miniWECC system is a reduced order representation of the western interconnection used for damping control analysis. Its derivation was based on a desire to create a lower complexity, linearized representation of the western North American power system while retaining the same characteristics as the full order system, allowing for study using software such as PST and PSLF. It has been thoroughly validated in previous studies [13]. It consists of 122 buses and 33 machines. Its one line diagram is shown in Figure 11. Similarly to the KRK system study, we co-located PV generation with all but one of the conventional generation sources and used the solar fraction parameter to shift generation from the conventional sources to the PV sources while proportionally reducing synchronous machine inertia. The system eigenvalue map resulting from the PV generation sweep is shown in Figure 12. A zoomed-in version focusing on lightly damped, oscillatory modes is also shown. (Note: The PV% only goes up to 70% in these sweeps because larger values estimates the existence of eigenvalues in the right-half plane.)

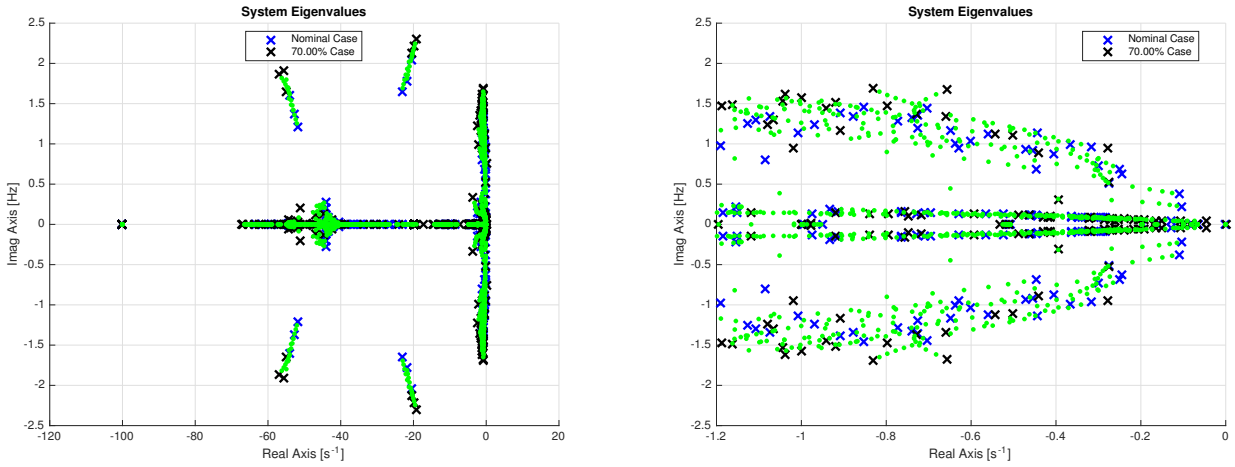

Figure 12: System eigenvalue sweep map for miniWECC. Right: zoom-in of the lightly damped modes from the left.

In the KRK system, we observed a decline in stiffness ratio as the solar fraction increased. In the miniWECC system, we actually observe a static stiffness ratio until it increases at 70% PV (c.f. Figure 13). Since the maximum decay rate in the system remains fixed regardless of PV%, this indicates that at least one eigenvalue (pair) is drifting right with increased PV%, causing the increase in stiffness ratio. This is supported by the appearance of unstable modes during a sweep up to 90% PV. Hence, it would be impossible to perform dynamic simulations using this test case as is — the operating point and/or controls would need to be changed/implemented to support high penetrations of PV generation.

The system described by the miniWECC case has been analyzed in the past and has several well-known modes that have been identified and named [13]. We aimed to identify these modes in this section using PST's linearization routine as well as in Section 3.5 using mode estimation via time domain simulations. The following figures are the compass plots of a selection of these modes at different solar penetration levels. Each vector in the compass plots is the machine speed of the synchronous machine located at the labeled location. The vectors are normalized and referenced in each plot such that the machine speed with the largest participation factor serves as the reference vector $1 + j0$. The remaining vectors displayed are assigned colors depending on their phase relative to the reference vector: the closer to π the vector is, the closer to indigo and further away from red it is (using a "jet" colormap). The state names are based on

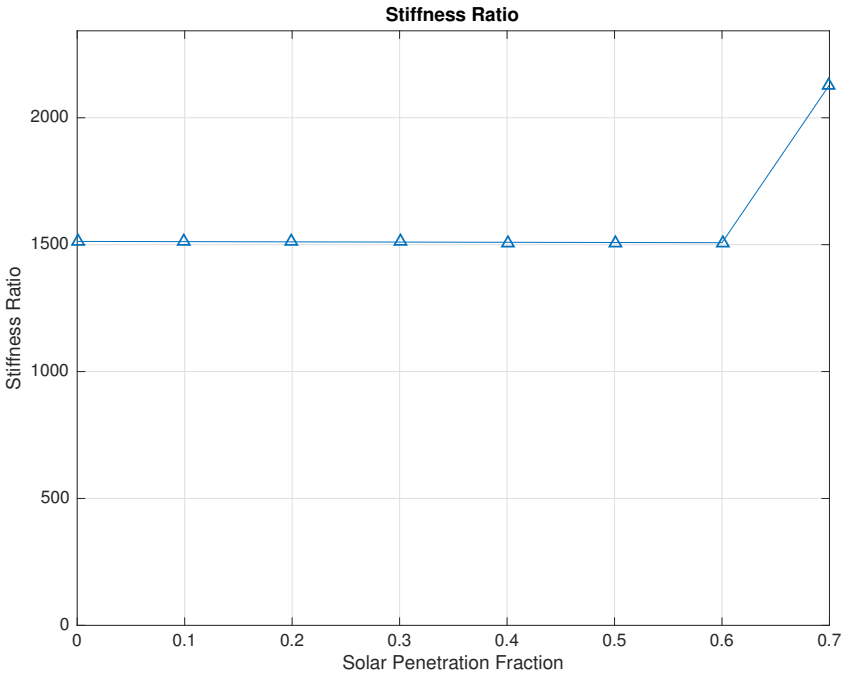

Figure 13: Stiffness ratio against PV%.

their geographical locations.

North-South Mode A North-South Mode A, nominally at 0.25 Hz, is characterized by the northern half of the miniWECC system swinging against the southern half [13].

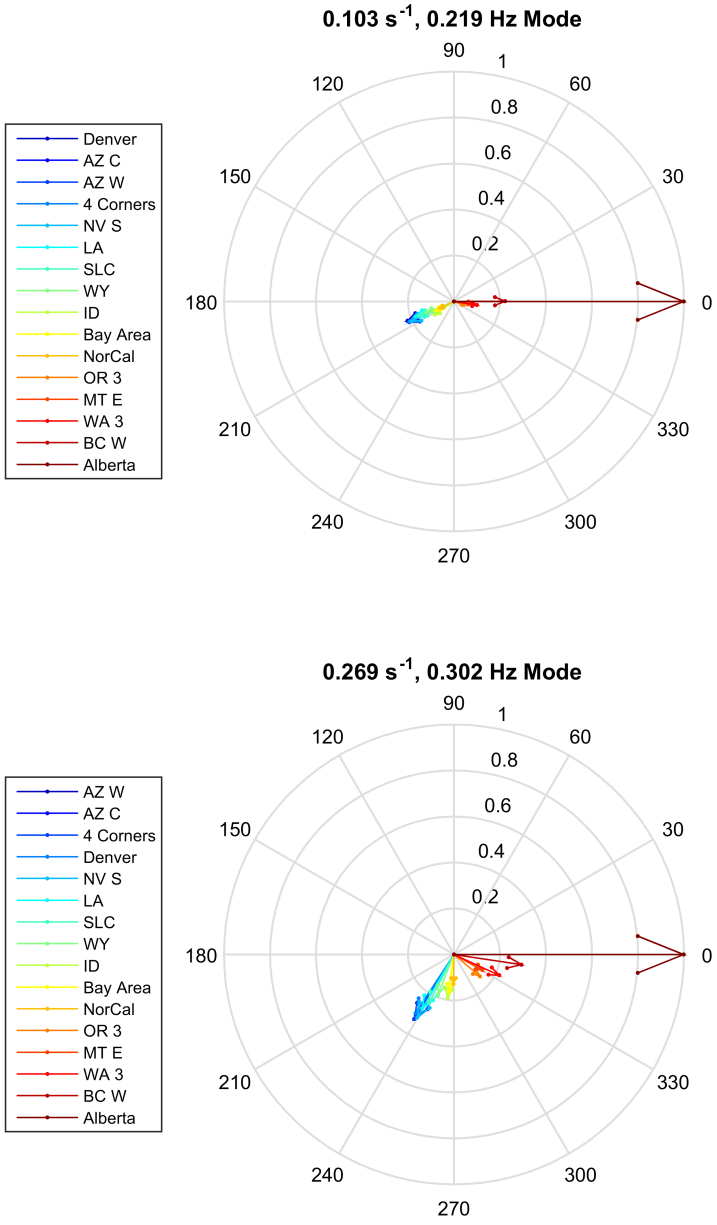

Figure 14: North-South Mode A. (top: base case, bottom: 50% PV)

North-South Mode B North-South Mode B, nominally at 0.4 Hz, is characterized by Alberta swinging against BC and the northern US, which is also swinging against the rest of the system [13].

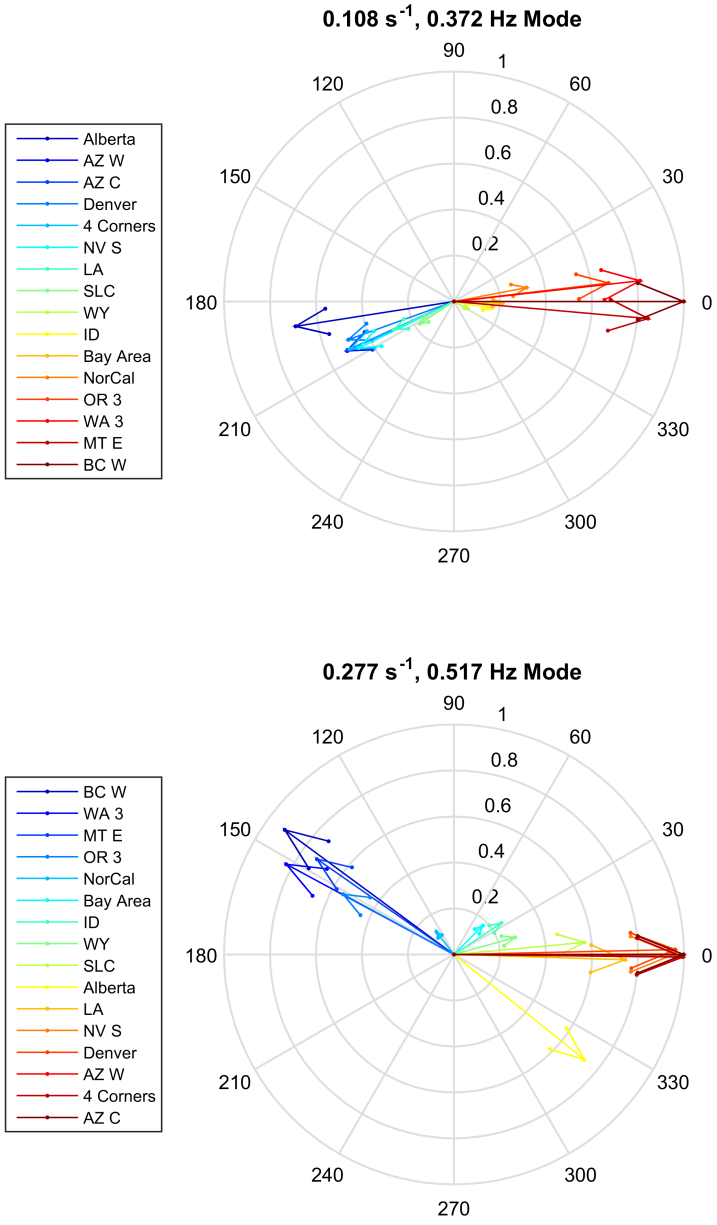

Figure 15: North-South Mode B. (top: base case, bottom: 50% PV)

Observations Using the base case analysis, the frequencies estimated of the North-South modes is in line with what is described in [13], subject to differences in operating conditions. We also tracked the damping ratio of these modes as a function of PV%; the results are shown in Tables 2 and 3.

Table 2: Damping ratios for North-South Mode A in the miniWECC system.

PV%	α [$\mathbf{s}^{(-1)}$]	**f [Hz]**	ξ [%]
0%	0.103	0.219	7.5%
25%	0.143	0.250	9.1%
50%	0.269	0.302	14.0%
60%	0.395	0.316	19.5%

Table 3: Damping ratios for North-South Mode B in the miniWECC system.

PV%	α [$\mathbf{s}^{(-1)}$]	**f [Hz]**	ξ [%]
0%	0.108	0.372	4.6%
25%	0.163	0.423	6.1%
50%	0.277	0.517	8.5%
60%	0.311	0.603	8.2%

The estimated damping ratios for North-South Mode A and B for the base case are in line with the reported ranges of 10-15% and 5-10%, respectively [13]. With increased PV%, the mode shapes of these two modes evolves such that the states become slightly closer in both magnitude and phase. This coincides with the increase in damping ratios of the modes.

3.3.3 Impact of stiffness on numerical integration scheme selection

For a comprehensive analysis of power system eigenvalues, we used a 16 machine, 68 bus system included with PST. This particular system made use of a subtransient reactance model for its machines, IEEE type 1 DC excitation systems, power system stabilizers, and induction motor loads. Having this variety of dynamic models ensures that we can observe a myriad of eigenvalues that one may have in any given power system model. Furthermore, we augmented the model by adding PV generation to all but one of the generation buses; this allowed us to study how increased PV penetration would affect this variety of eigenvalues.

We used PST's linearization routines to estimate the eigenvalues at discrete levels of solar fraction values, starting from a nominal case of 0% PV up to 90% PV; experimentally, we determined that either the linearization or power flow would fail beyond 90% PV for this particular case. We then plotted all of the computed eigenvalues simultaneously to illustrate the trajectory of eigenvalues as PV penetration increased. The results are shown in Figure 16.

The estimated eigenvalues constitute a wide variety of frequencies and decay rates. This large range of decay rates would seem to indicate a large stiffness ratio. To confirm, we computed the stiffness ratio across solar fraction values, shown in Figure 17.

Notably, there doesn't seem to be any correlation of stiffness ratio with PV generation as hypothesized. To determine why, we plotted min/max decay rate eigenvalues against solar fraction. While the smallest eigenvalue decay rate varied erratically with PV%, the largest eigenvalue decay rate remained fixed (c.f.

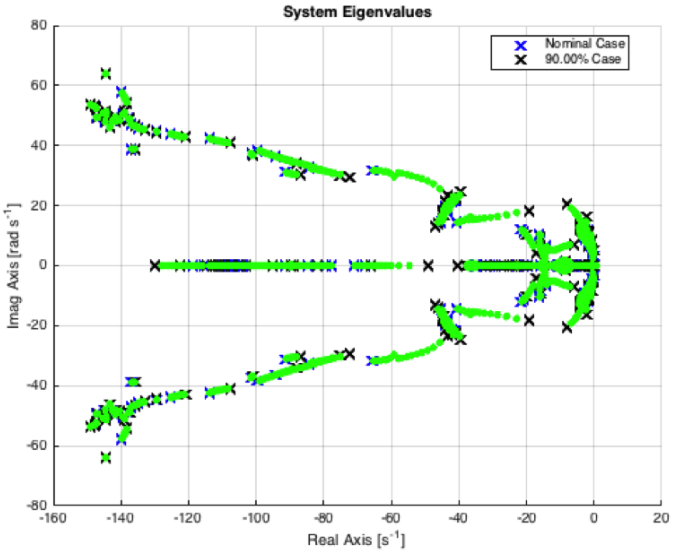

Figure 16: System eigenvalue sweep map for 68 bus system.

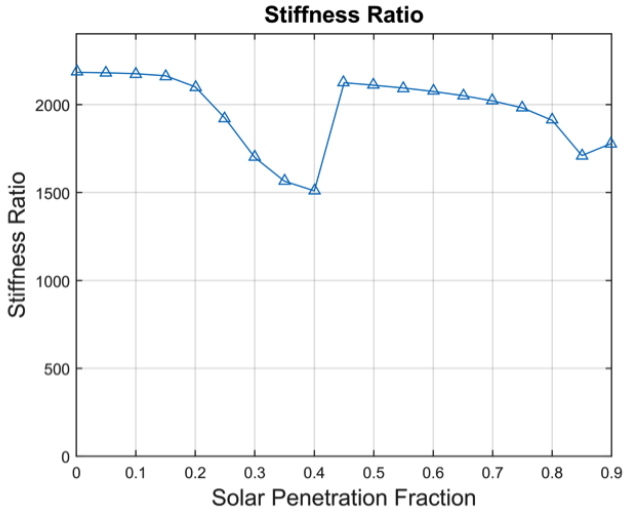

Figure 17: Computed stiffness ratio of 68 bus system across different penetration levels.

Figure 18) . Throughout the stiffness analysis of other test cases, this trend typically held. The fastest dynamics in these systems tended to be unaffected by PV%. While the slowest dynamics in these systems were affected by PV%, their relationship cannot really be generalized. Therefore, we found it unrealistic to correlate system stiffness (using stiffness ratio) with PV penetration.

While these results on their own are illuminating, we wanted our analysis to be more generalizable, not just specific to this particular test case. We analyzed PST's code to determine the specifics of these eigenvalues. We wanted to know what parts of the power system are responsible for which eigenvalues. With this information, we could predict the arrangement of eigenvalues of any given test case — we called

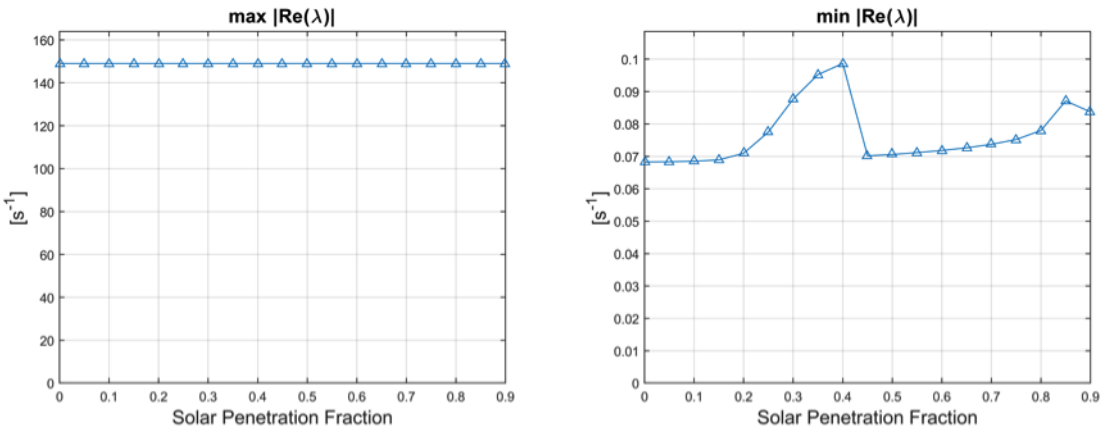

Figure 18: Mode decay rates used in stiffness ratio calculations for 68 bus system.

this the "system eigenvalue topology" — based on the dynamic models present in the case specification. In order to do this, we examined the participation factors of each eigenvalue. The participation factor is defined as:

$$p_{ik} = l_k^i r_k^i \tag{3.13}$$

where l^i and r^i are the left and right eigenvectors, respectively, of the ith eigenvalue and k refers to the kth state. An interpretation of the participation factor p_{ik} is the relative participation of the kth state in the ith mode [14]. Hence, a large participation factor implies that that particular state is largely responsible for that particular mode. By relating which state indices mapped to which dynamic model states, we were able to proceed with our analysis.

We studied our 16 machine test case and examined the estimated eigenvalues. We observed that there were definitive regions of the complex eigenvalue plane that would be populated if specific dynamic models were present. The results of our analysis are shown in Figure 19.

These results are interesting in the context of considering numerical integration methods. Typically, the "simplest" PST test cases consisted of machine models and excitation systems. In these cases, we would not see high frequency modes like those of induction motor loads in the stiffness analysis. Furthermore, the fastest dynamics in the orange region tended to be unaffected by the increasing PV penetration. Therefore, it is unlikely that the requirements for dynamic simulation of systems with high PV penetration would change because of the presence of PV; it is more likely that the presence of certain dynamic models (e.g., induction motor loads) would be the driving force behind any changes in how these systems are simulated. We will discuss this in more detail when discussing numerical integration methods in the proceeding section.

3.4 Numerical Integration Scheme Analysis

In this study, we sought to propose suitable integration schemes for dynamic simulation over long time periods for high PV penetration scenarios. While stiffness analysis revealed that PV, as we have modeled, is not a directly significant driver in integrator selection, we observed that it may become significant depending on the types of controls implemented and modeled for PV (as seen in the PSLF example.) Therefore, in the context of this report, this section primarily addresses the extended-term simulation component of the study but the comparisons made here will apply depending on how PV is modeled.

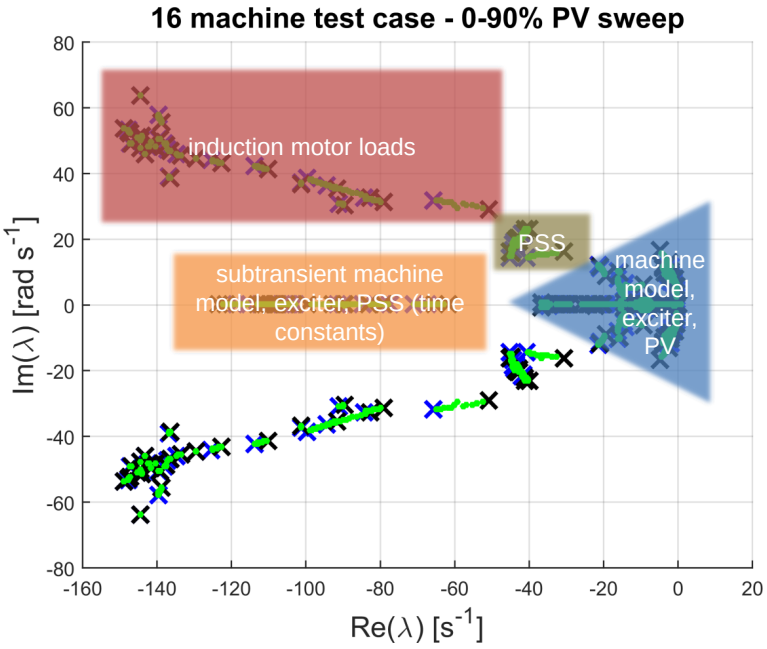

Figure 19: System eigenvalue map for 68 bus system with typical eigenvalue locations for common power system model components.

One method of increasing extended-term simulation viability is to increase the step size of the integrator. As we have demonstrated, we are limited in this regard by numerical stability. For implicit methods, numerical stability is not much of a concern as A-stability is a possibility whereas it is not for explicit methods. However, implicit methods tend to be relatively difficult to implement and computationally expensive. For improved accuracy, we would also like to consider higher order numerical methods but likewise they come at the cost of increased computation and memory needs. Although computing power has made large strides since the inception of dynamic simulation software, there is still significant effort expended in reducing simulation runtimes to close or faster than real time. For large systems, simulating even minute-long durations produces gigabytes of data that scale with system size, simulation step size, and simulation duration. Reductions in this amount of data are immense for both storage and transfer purposes for research.

While we propose that the trapezoidal rule is a suitable choice for the goals of this study, it is difficult to analyze and comes with the aforementioned issues due to being an implicit method. Thus, our focus shifted to viable explicit method candidates, including predictor-corrector methods. In our initial investigations with PST, we learned that the toolbox relies upon a 2nd-order accurate predictor-corrector algorithm known as Heun's method [15]. This integration scheme uses the forward Euler scheme as its predictor and the trapezoidal rule as its corrector. To achieve the goals of this study, we investigated the behavior of the integration scheme employed by PSLF and PSS/E, the two-step Adams-Bashforth method (AB-2). Based on the analysis of system stiffness and other computational requirements, we identified the 4th-order accurate Crane-Klopfenstein (CK-4) predictor-corrector scheme as a candidate explicit integration scheme [16]. The CK-4 integration scheme possesses a high order of accuracy and excellent stability characteristics

while being straightforward to implement in software. As a baseline, we included the simple Forward Euler integration scheme although it is not a real candidate due to its limited stability properties and poor accuracy.

The selection of a numerical integration scheme for a dynamical system simulation platform is driven by a number of factors. In particular, there exists a tradeoff chiefly among integrator accuracy, computational and memory burden, ease of implementation, and numerical stability properties. Typically, the first decision when selecting an integration scheme is deciding between using an implicit or explicit scheme. In general, explicit schemes are easier to implement at the cost of accuracy and numerical stability [17] whereas comparable implicit schemes improve in these facets at the cost of ease of implementation and computational burden. For example, a typical explicit integration scheme can be dynamical system agnostic and be written solely in terms of already calculated state derivatives. On the other hand, an implicit integration scheme usually requires solving a set of nonlinear equations which involves significantly more computation. In this section, we will be comparing four explicit integration schemes:

- Forward Euler method
- Two-step Adams-Bashforth method
- Heun's method
- Four-step Crane-Klopfenstein method

We will examine how the schemes differ in computational burdens both analytically and using experimental benchmarks. We will also be examining accuracy properties in terms of order of accuracy, local truncation error, and accumulated error. Finally, we will look at how the schemes differ in numerical stability using regions of absolute stability. Using these analyses, we will discuss the tradeoff in selecting among these particular schemes in the context of power system simulation.

3.4.1 Computational considerations

When looking at the computational burden of integration schemes, we primarily look at the number of rate calls and number of memory storages and calls per time step or iteration. Rate calls are the execution of the routine to compute the derivatives of the state variables in the system. Typically, this is only once per iteration for standard explicit integration schemes but predictor-corrector schemes can include numerous rate calls. Memory access is mostly tied to the order of the integration scheme but can also increase depending on the implementation of a predictor-corrector scheme. We will define each integration scheme to be examined and analyze how each is computationally taxing. Unless explicitly noted, all analysis is done assuming a fixed time step h.

Forward Euler method The Forward Euler method is a simple first order integration scheme. It is defined as:

$$y_{n+1} = y_n + hf_n \tag{3.14}$$

where $f_n = \frac{\mathrm{d}}{\mathrm{d}t} y_n$ and h is the (fixed) time step. At each iteration of this method, there is a single rate call. There is a single explicit memory call but more may be necessary depending on the state derivative computation. (We will ignore this moving forward because state derivative computation is invariant of the integration scheme of choice.)

Two-step Adams-Bashforth method The two-step Adams-Bashforth method (AB-2) is a second order integration scheme that is employed by a number of commercial power system simulation software vendors. It is defined as:

$$y_{n+1} = y_n + \frac{h}{2}\left(3f_n - f_{n-1}\right) \tag{3.15}$$

At each iteration, there is a single rate call. Like the Forward Euler method, there is a single memory call of the current state variable. However, there is also a memory call of a previous time step's state derivative due to AB-2 being a second order method.

Heun's method Heun's method is the first of the two predictor-corrector methods under consideration. The predictor is a simple Forward Euler step:

$$p_{n+1} = y_n + hf_n(t_n, y_n) \tag{3.16}$$

The corrector is a trapezoidal rule step:

$$y_{n+1} = y_n + \frac{h}{2}\left(\frac{\mathrm{d}}{\mathrm{d}t}p_{n+1} - f_n(t_n, y_n)\right) \tag{3.17}$$

where:

$$\frac{\mathrm{d}}{\mathrm{d}t}p_{n+1} = f(t_{n+1}, p_{n+1}) \tag{3.18}$$

is the state derivative computed using the predicted state variable value. This method is sometimes called the explicit trapezoidal rule due to the corrector step. In the predictor step, there is a single memory call (state variable) and a single rate call. With the addition of the corrector step, there are two memory calls (the state variable and the state derivative computed in the predictor step) and an additional rate call to compute the state derivative using the predicted state variable value. This totals three memory calls and two rate calls per iteration.

Four-step Crane-Klopfenstein method The four-step Crane-Klopfenstein method (CK-4) is a fourth order predictor-corrector method [16]. The predictor is defined as:

$$p_{n+1} = a_2y_n + b_1y_{n-1} + c_1y_{n-2} + d_1y_{n-3} + h(e_1f_n + q_1f_{n-1} + g_1f_{n-2} + k_1f_{n-3}) \tag{3.19}$$

The corrector is defined as:

$$y_{n+1} = a_2y_n + b_2y_{n-1} + c_2y_{n-2} + h(d_2\frac{\mathrm{d}}{\mathrm{d}t}p_{n+1} + e_2f_n + q_2f_{n-1} + g_2f_{n-2}) \tag{3.20}$$

The coefficients were numerically computed and are summarized in Table 4.

The predictor step requires four memory calls for the state variables, three memory calls for the state derivatives, and one rate call for the current time step state derivative. The corrector step requires three memory calls for the state variables, three memory calls for the state derivatives, and one rate call for the predicted state derivative. This totals 13 memory calls and two rate calls per iteration, a substantial increase over Heun's method. A summary of the rate and memory call counts is shown in Table 5.

Table 4: Four-step Crane-Klopfenstein method coefficients.

$a_1 = 1.547652$	$a_2 = 1$
$b_1 = -1.867503$	$b_2 = 0$
$c_1 = 2.017204$	$c_2 = 0$
$d_1 = -0.697353$	$d_2 = 0.375$
$e_1 = 2.002247$	$e_2 = 0.791666667$
$f_1 = -2.03169$	$f_2 = -0.208333333$
$g_1 = 1.818609$	$g_2 = 0.0416666667$
$k_1 = -0.71432$	

Table 5: Summarizing the number of memory and rate calls for various integration techniques.

	Memory calls	Rate calls
Forward Euler	1	1
AB-2	2	1
Heun's method	3	2
CK-4	13	2

Integrator performance benchmark tests In order to demonstrate how computational differences among the integrators affect real time performance, we developed a benchmarking tool in MATLAB using our previously mentioned 2nd order ODE test platform. We simulated a step response using each of the integrators of interest. We performed a 100 second simulation for 3 different step sizes; this means that the number of steps in each simulation varied depending on the step size. We simulated 100 different systems in which the eigenvalue pair location each time was randomized but within the region of absolute stability for all integrators. The simulations were performed on a laptop computer with an Intel Core i7-4600U CPU 2.1 GHz and 8.00 GB of RAM running Windows 7. The results, in seconds, are shown in Table 6.

Table 6: Total time taken to complete 100 simulations for various step sizes.

Total Time [s]			
	$h = \frac{1}{4}$ **cycle**	$h = \frac{1}{2}$ **cycle**	$h = 1$ **cycle**
Forward Euler	19.50729	9.320980	4.744207
AB-2	22.70859	10.77197	5.325676
Heun's method	33.04143	15.54170	7.731683
CK-4	50.57874	23.36001	11.599648

In order to see how average simulation time scaled with step size/step count, we did a similar experiment with a broader range of step sizes. The results are shown in Figure 20.

We see that average simulation time scales exponentially with step count. On the other hand, as one would expect, average time per iteration is invariant of step size. These results are more interesting in the context of the other factors driving integrator selection. For example, AB-2 is commonly used for power systems simulation software and has good computational performance for the standard quarter cycle step size ($\sim$.004 s). As we will present later, the contender CK-4 has similar, if not more desirable,

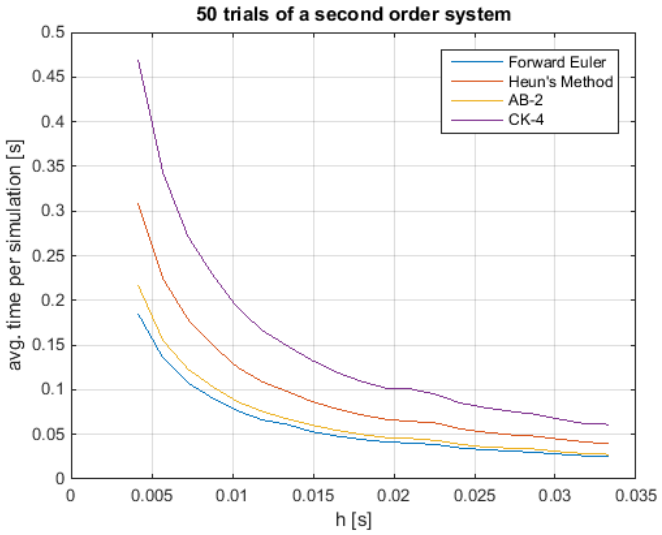

Figure 20: Average time per 100s. simulation taken over 50 trials.

numerical stability properties as AB-2 at the full cycle step size (∼.016 s). If we extrapolate from the previous experiment, CK-4 is faster than AB-2 when considering the different step size. If the accuracy is comparable or better for CK-4 at this larger step size, it would favor selecting CK-4 for simulation.

3.4.2 Accuracy considerations

A numerical integration scheme is typically not useful if it is inaccurate. Schemes are typically classified in terms of accuracy by their "order"; this nomenclature is derived from the method's local truncation error, an analytical estimate of how much an integration method differs from the true solution on a step-by-step basis. In this section, we will present two of the metrics we used to examine integrator accuracy and present some experimental results to characterize the four aforementioned integration schemes.

Local truncation error (LTE) We define local truncation error, τ_n, at each time step n as the difference between the true function value $y(t_n)$ and the function value according to the integration scheme, y_n:

$$\tau_n = y(t_n) - y_n \tag{3.21}$$

This quantity is computed assuming that the estimated y_n is calculated based on exact information, i.e., $y_{n-k} = y(t_{n-k}) \; \forall \; k > 0$. In other words, it is assumed that all previous iterations of the integration scheme are exactly correct. We can compute τ_n for various integration schemes in order to get a sense of their order of accuracy. For example, we can estimate order of accuracy as related to step size h and even rank different schemes that have the same order of accuracy.

In general, according to the orders of accuracy and coefficients of the leading error terms, we expect that Heun's > AB-2 > Forward Euler in terms of order of accuracy. We expect that AB-2 and Heun's method perform very similarly for a given system and both to perform better than the Forward Euler method. Additionally, with CK-4 being a fourth order method, we expect it to be the most accurate in terms of local truncation error.

In a stable system, assuming that the system eigenvalues are in the region of absolute stability for all numerical methods, we expect that the solution for all schemes to converge to some final value determined by system parameters. Consequently, we expect the local truncation error for each method to converge to 0 in that scenario and that the order of accuracy correlates with the rate of convergence. We illustrate these observations with some simulated examples.

Example: Second order ODE We consider the following 2nd order ODE:

$$\frac{\mathrm{d}^2}{\mathrm{d}t^2}y(t) + b_0\frac{\mathrm{d}}{\mathrm{d}t}y(t) + k_0 y(t) = f(t) \tag{3.22}$$

with $y(0) = 0$ and $\frac{\mathrm{d}}{\mathrm{d}t}y(0) = 0$. The characteristic constants are $b_0 = 2\alpha_0$ and $k_0 = \alpha_0^2 + \omega_0^2$ and the system eigenvalue pair is located at $s = -\alpha_0 \pm j\omega_0$. We only consider $\alpha_0 > 0$ and thus are only considering underdamped systems with oscillatory responses. The forcing function $f(t)$ is the unit step function, $u(t)$. It can be verified that the analytic solution to this ODE is:

$$y(t) = \frac{1}{k_0}\left[1 - e^{-\alpha_0 t}\cos\left(\omega_0 t\right)\right]u(t) \tag{3.23}$$

Case 1: $\alpha_0 = 0.5, \omega_0 = 2$ This example illustrates an underdamped system where all three integration schemes are numerically stable. The step size h is chosen to be 0.1. The integration results are more obvious in their differences among the schemes although all schemes do eventually converge to the true solution.

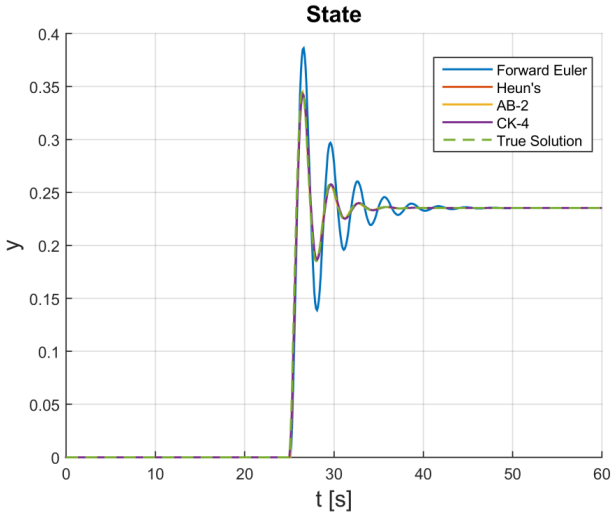

Figure 21: Integrated results compared to the true solution for Case 1. We can start to observe more apparent accuracy differences.

The local truncation error illustrates the major differences. We observe that the first order scheme has a nontrivially larger maximum LTE in addition to converging more slowly to zero LTE as compared to the higher order schemes. In this example, the accumulated error is more indicative of the differences in orders of accuracy among the schemes. Although all schemes have LTE that eventually converge to 0,

the accumulated error bound for each is different. The higher order schemes' accumulated errors converge more quickly to similar, lesser values as compared to the first order scheme. However, we notice that the higher order CK-4 method has a marginally larger steady state accumulated error compared to the second order schemes in addition to marginally larger local truncation error at earlier time steps. This does not match the concept of order of accuracy as presented previously. Through experimentation, we found that the CK-4 tends to perform more accurately compared to the second order methods when the eigenvalue pair has a higher frequency.

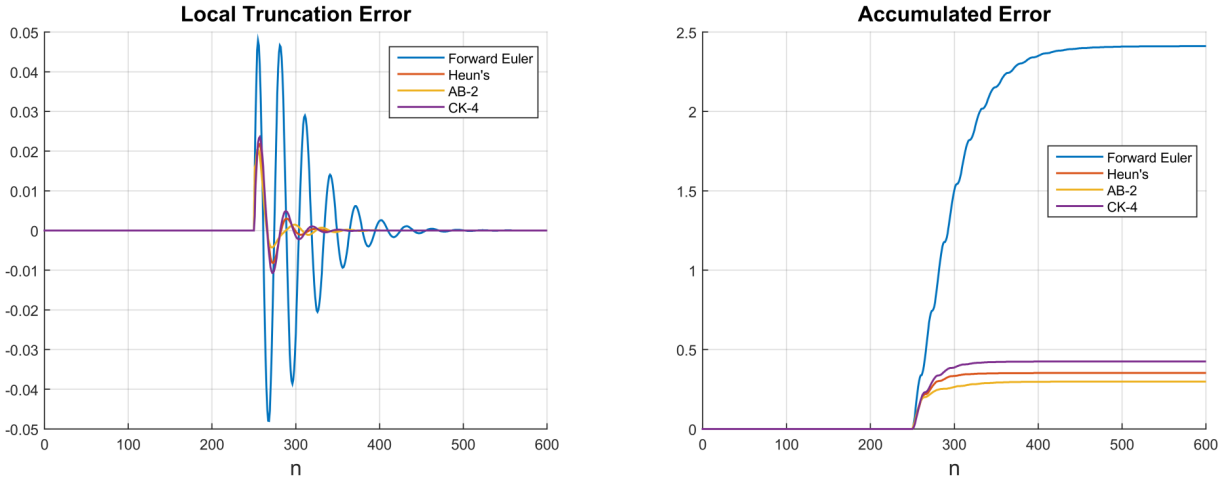

Figure 22: Local truncation and accumulated error for Case 1.

Case 2: $\alpha_0 = 0.5, \omega_0 = 5$ In this example, we keep the eigenvalue decay rate the same but increase the frequency. We remove the Forward Euler method results because we've already demonstrated its poor accuracy performance and because it is numerically unstable for the time step and eigenvalue pair location chosen. The results are shown in Figures 23 and 24.

From the state variable calculations, we can observe how the higher order integration methods start to differ. While CK-4 has no trouble keeping up with the true solution, the two second order schemes start to desync and become out of phase with the true solution within cycles. This manifests into a much slower convergence to zero local truncation error compared to CK-4 and, consequently, a larger steady state accumulated error. In the previous example, we saw an approximate 100% increase in accumulated error between CK-4 and AB-2; here we observe over a sevenfold increase in accumulated error from AB-2 to CK-4.

Observations Analytically, it is unclear why there is such a disparity between these two examples in terms of integrator relative performance. Depending on the dynamical system of interest, it might be worth considering these idiosyncrasies when selecting an integration scheme. However, it is worth noting that the higher order integration schemes seem to perform better in the relative error sense.

The most substantial metric for examining local/global truncation error is far and away the order of accuracy. Among integration schemes with the same order of accuracy, the differences in LTE/accumulated error and convergence to the true solution are minute, regardless of the coefficient on the leading term of

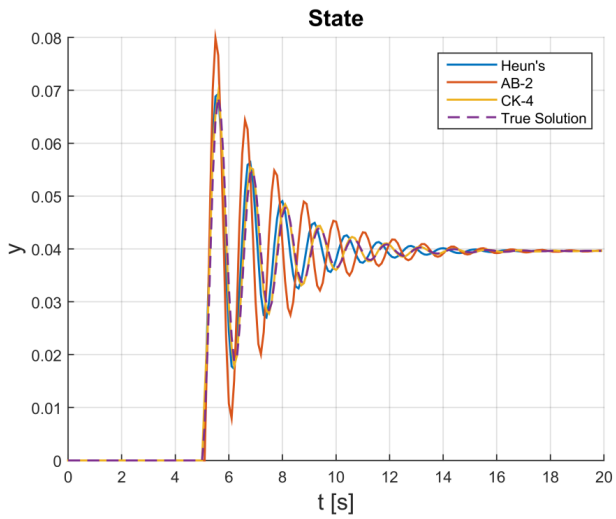

Figure 23: Integrated results compared to the true solution for Case 2. We can start to observe more apparent accuracy differences even among higher order schemes.

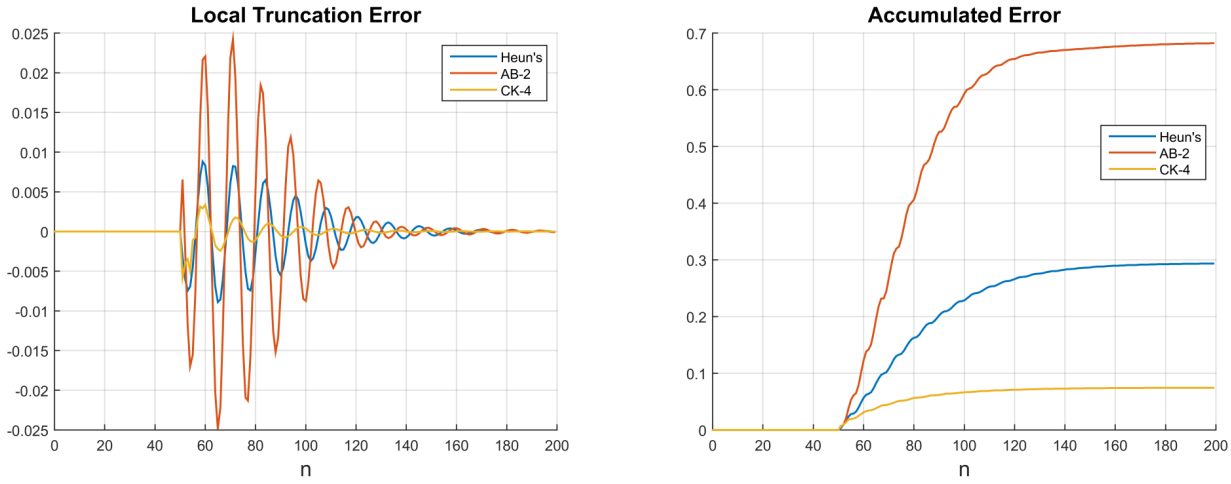

Figure 24: Local truncation and accumulated error for Case 2.

the LTE. Admittedly, this is based on a very small sample size of integration schemes. The differences among integration schemes with different orders of accuracy, however, are significant.

The seemingly obvious choice is to choose the highest order of accuracy integration scheme for the best integration performance. However, as we observed, the computational burden for higher order schemes increases at a superlinear rate as method order increases. In the next section, we will examine the final facet of numerical stability and summarily illustrate the tradeoffs when selecting an integration scheme.

3.4.3 Numerical stability considerations

Previously, we touched on the general concepts of relative and absolute stability in the context of numerical integration methods. In particular, we looked at the relationship between system dynamic stability and

integrator numerical stability in terms of system eigenvalue locations. In this section, we will revisit these concepts, specifically for the four integration methods under investigation.

Region of absolute stability The procedure for calculating the region of absolute stability was outlined as follows:

1. State the recurrence relation determined by the numerical method.
2. Compute and solve the characteristic polynomial for its roots.
3. The region of absolute stability is the region in which all roots of the characteristic polynomial have a magnitude strictly less than unity.

This region is defined in the $\bar{h} = h\lambda$ complex plane, where h is the step size in seconds and λ is the complex eigenvalue. Hence, the region needs to be scaled by the step size in order to compare it to system eigenvalues. For lower order multistep methods, deriving the region of absolute stability analytically is tractable. For higher order methods (> 2), computing the region needs to be done numerically. Figure 25 shows the regions of absolute stability for the four integration methods of interest in the $h\lambda$-plane.

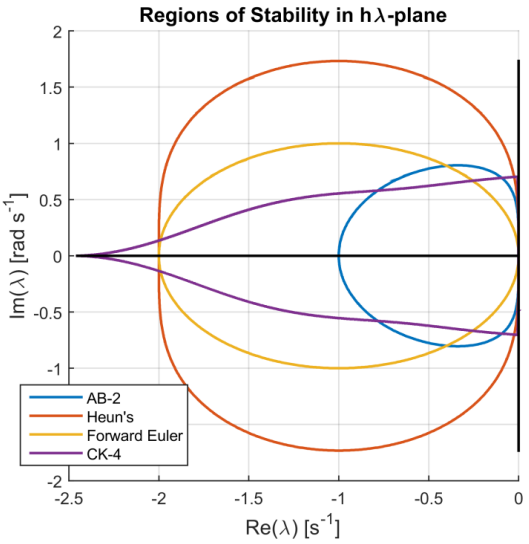

Figure 25: Region of absolute stability for the integration methods in the $h\lambda$-plane.

All methods include some subset of the left plane, which encompasses all eigenvalues for dynamically stable systems. Here we can observe the characteristic shape of CK-4: thin near the $j\omega$-axis like AB-2, but extends out far along the real axis like Heun's method but even further into a characteristic cusp.

In Figure 26, we scaled the regions of absolute stability to the s-plane for two step sizes of interest — quarter cycle and full cycle. As we observed in the stiffness analysis for the two cases, the limiting eigenvalues for system stiffness tended to be those related to the dynamics of the exciters; in particular, they were related to the time constants of the voltage transducers in the exciter models. For time constants on the order of 10 to 20 ms, the corresponding system eigenvalues were located at -50 to -100 on the real axis. For a time step of a quarter cycle, these eigenvalues fit comfortably in the region of absolute stability

for all integrators, including the oft-used AB-2. However, for a full cycle time step, AB-2 begins to run into trouble numerically due to its relatively truncated region of absolute stability. Due to the characteristic cusp of CK-4, one can imagine that if the limiting eigenvalues are known ahead of time, if CK-4 is used to integrate, then the time step can be selected precisely such that the limiting eigenvalues fit within the region of absolute stability.

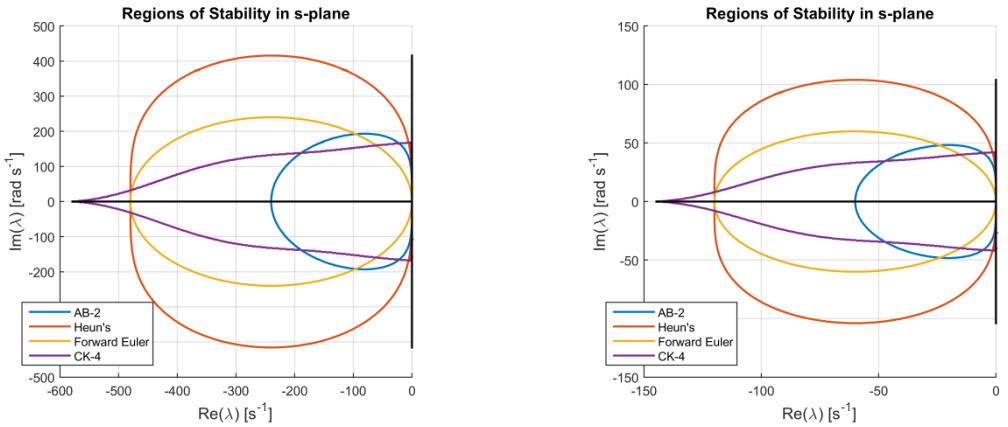

Figure 26: Regions of absolute stability for two different step sizes. (left: quarter cycle, right: full cycle)

Numerical oscillations Previously, we demonstrated what effect absolute stability has on numerical integration. Although absolute stability guarantees the simulated solution will eventually converge to the true solution, this does not exclude less than desirable phenomena such as numerical oscillation from occurring. Empirically, numerical oscillation directly correlates with proximity to the region of absolute stability boundary. As system eigenvalues encroach on the boundary from within the region, numerical oscillation severity seems to increase. Using the previous example, we can demonstrate this phenomenon. The step size of choice and the system eigenvalue locations create a situation in which the system eigenvalues are very near the boundary of the region of absolute stability for AB-2.

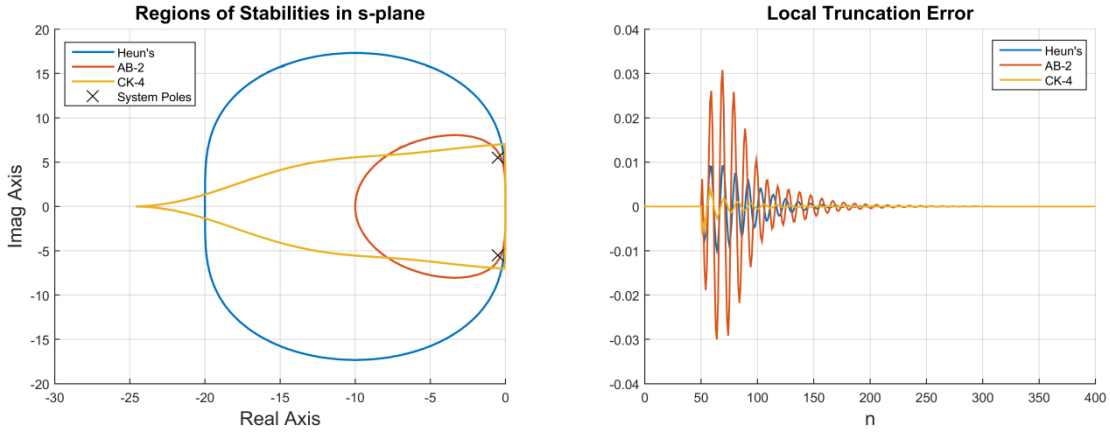

Figure 27: System eigenvalue map and LTE for corresponding simulation.

Refer to the previous section to see the calculated system state. While the solution using AB-2 eventually does converge to zero local error and the true final value, the state variable time series as simulated is fundamentally different from the true solution. The decay rate is significantly slower compared to the more accurate simulated solutions and it is significantly out of phase with the true solution. Furthermore, there is significant overshoot and undershoot as simulated as well as a slight frequency depression. These issues can potentially cause false alarms if, for example, there are controls that respond to voltage limits or frequency dips. So while absolute stability should be the primary factor when considering the numerical stability of potential integrators, the actual "effective" region of absolute stability is most likely smaller than depicted due to numerical oscillation concerns.

Numerical stability demonstrations with PST By modifying the PST code, we implemented AB-2 and CK-4 as integrator choices in PST. While simple second order systems possess the transparency that makes it easy to compare aspects of numerical integration such as accuracy, this analysis was ultimately for selecting an integration scheme for power system simulation. In the next few examples, we will demonstrate how numerical stability affects dynamic simulation.

Example: Instability of AB-2 We used the KRK system with half of the exciters having voltage transducer time constants of 10 ms, resulting in eigenvalues at approximately -100 s^{-1}. We fixed the integrator time step at a full cycle; it can be verified that this causes the exciter system eigenvalues to lie outside of AB-2's region of absolute stability but inside those of Heun's method and CK-4 (c.f. Figure 26). To excite system modes, we simulated a three-phase fault like what was done in the time domain analysis.

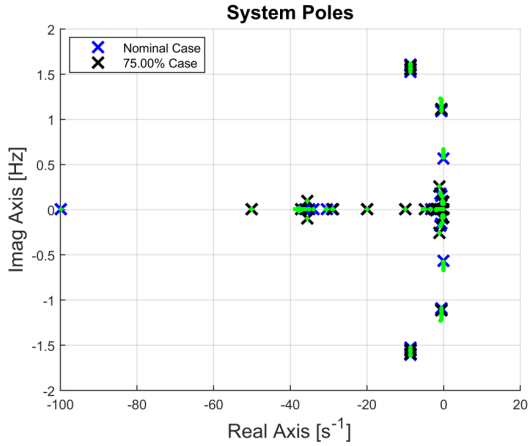

Figure 28: System eigenvalue map for transient response simulation.

Figure 29 shows the simulated responses using Heun's method and CK-4. Qualitatively, they appear similar to the response that one would expect. Figure 30 shows the simulated response using AB-2. The simulation actually froze and failed to complete the entire simulation duration (30 seconds). We can observe that the simulated solution is already showing divergent behavior before the software hung.

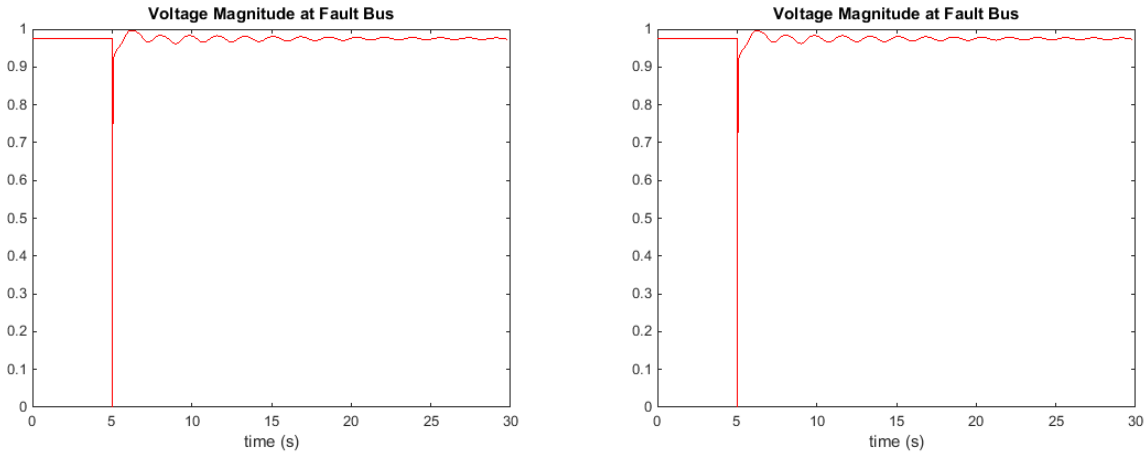

Figure 29: Transient response as simulated using Heun's method and CK-4.

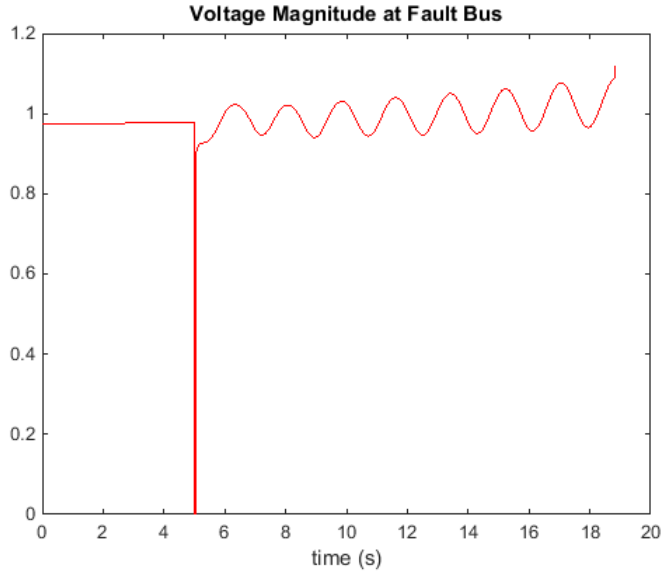

Figure 30: Transient response as simulated using AB-2.

3.4.4 Power system eigenvalue topology and selecting an integrator

With numerical stability as the priority criterion for selecting an integrator, it is vital to understand the general eigenvalue topology for the typical power system to be simulated. In general, power system models typically contain the same component dynamic models with associated system eigenvalues in the same region of the complex plane; there is variation in eigenvalue location due to actual parameter values. To illustrate this point, we used a 16 machine test case containing 29 induction motor loads. In Section 3.3, we presented a system eigenvalue topology map derived from this test system, shown again in Figure 31.

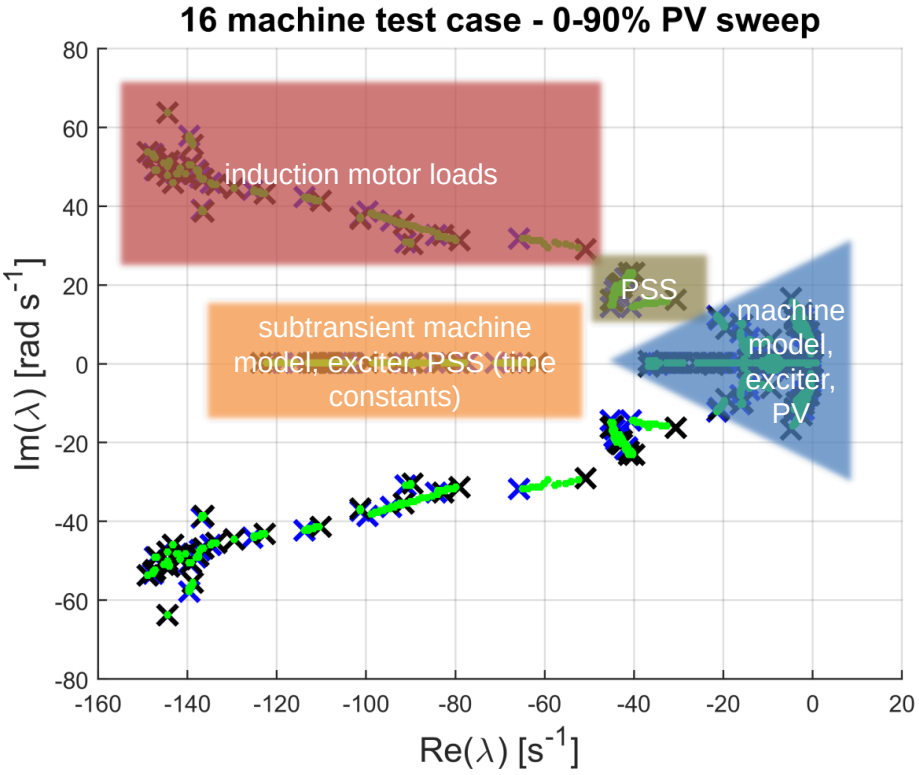

Figure 31: System eigenvalue map for 68 bus system with typical eigenvalue locations for common power system model components.

Using the methodology for mode identification and state association used in Section 3.3, we annotated the eigenvalue map to indicate what dynamic models are associated with various regions in the complex eigenvalue plane. While the two example systems we analyzed in depth did not contain them, induction motor load models are most likely to restrict the selection of an integrator due to their fast decaying, high frequency modes. Most commonly, the time constants associated with transient and subtransient machine models, exciters, and PSS will stress the selection of an integrator and/or step size. The region annotated on the eigenvalue map is directly correlated to these time constants, which are typically in the 20 ms or smaller range. The dynamics associated with these time constants are far and away the fastest dynamics in power system models that do not contain induction motor loads. Due to region of absolute stability

shapes for typical explicit integration schemes, these time constants will most likely restrict how large the step size can be. The other two regions identified are highly unlikely to affect the choice of integrator and step size; these relatively slower decaying, low frequency modes will almost surely be well within the region of absolute stability for any integrator unless all of the aforementioned time constants happen to be very large. Additionally, the `pwrmod` model used to model PV current injections has associated eigenvalues at -20 s^{-1} due to 50 ms time constants. As noted previously, increased PV penetration, as modeled, has no definite effect on system stiffness. Integrator selection stress does not directly come from the presence of PV-related current injections, but rather from the tendency for system eigenvalues to drift left with increased PV penetration.

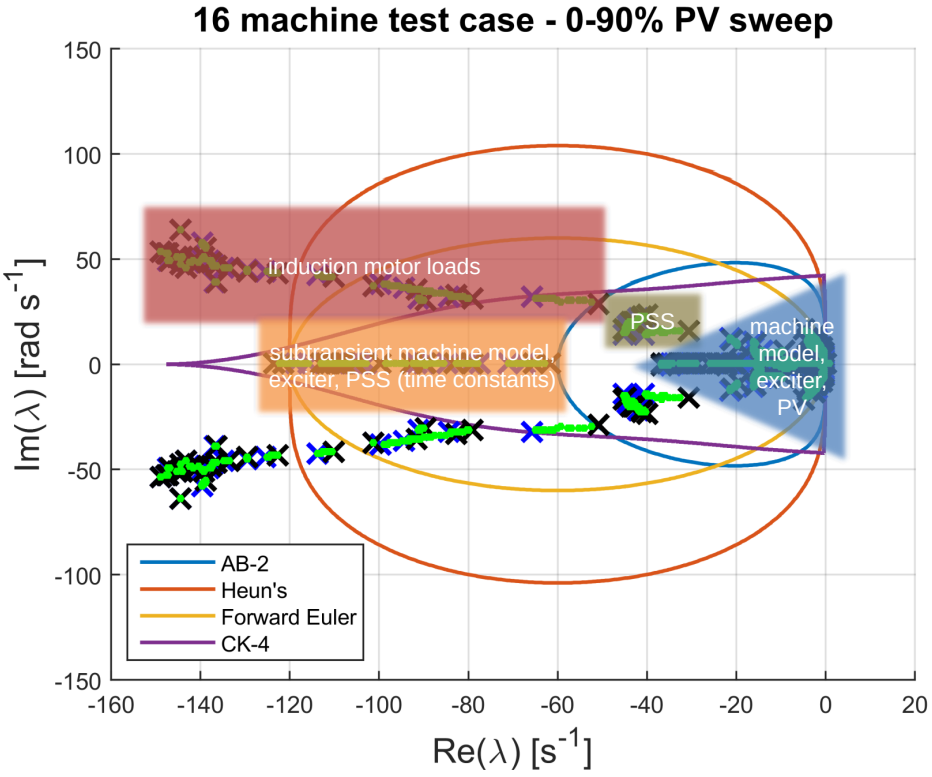

Figure 32: System eigenvalue topology with region of absolute stabilities $h = \frac{1}{60}$ s overlaid.

3.4.5 Conclusions

One of the reasons for considering different integrators for extended-term simulation of power systems with high PV penetration is that for very long simulation lengths, it is less feasible to use integrators with the oft-used quarter-cycle timestep due to computation speed and data storage bloat. Based on our analysis, the ubiquitous AB-2 with a quarter-cycle timestep is very capable for most power systems to be simulated and is perfectly suitable for shorter duration simulations. For simulations of durations exceeding the minute mark, increasing the timestep to, i.e., a full cycle would be a massive improvement in terms

of computation time and data storage management. Because of its unique numerical stability properties, we recommend CK-4 as an integrator because it tends to be highly compatible with many power system models; additionally, it gives the most real estate in terms of absolute stability where it matters for a given step size. As a result, one is most likely able to reduce the simulation step size using CK-4 than the other integrators. While this comes at the cost of additional computation time, based on our analysis, it might actually be faster to use CK-4 than other integrators because other integrators are more likely to require a smaller step size for numerical stability.

One drawback of using CK-4 is its thinner region of absolute stability in the frequency sense. From the example of the system with induction motor loads, this property tends to be problematic for CK-4 because of the existence of large decay rate, high frequency modes. The presence of these modes requires CK-4 to use a larger step size to be numerically stable when simulating this type of system and eliminates the advantage of CK-4. For this reason, we recommend using Heun's method as it contains much more bandwidth for a given step size. Figure 32 illustrates how the regions of stability at a full cycle time step compare to the archetypical system eigenvalue map.

In general, we recommend using small signal stability studies or having some knowledge of the dynamics of a power system to be simulated in order to make an intelligent selection of a numerical integration method. For general purpose, versatility, and safety, we recommend Heun's method because of its relatively large region of absolute stability, ease of implementation, and reasonable computational performance. For extended-term simulations, we recommend CK-4 whenever the characteristics of the power system model allow for it because of its potential to increase the fixed simulation step size and reduce the number of iterations and data storage required.

Table 7: Summary of integrator analysis; rankings based on a fixed step size.

Integrator	**Accuracy**	**Speed**	**Numerical stability**	**Implementation Ease**
Forward Euler	Worst	Fastest	2nd most space on real axis; 2nd most space on imaginary axis	Simpler; first order explicit method
Second order Adams-Bashforth	Comparable to CK-4	Close 2nd	Distant last for real axis; last for imaginary axis	Simpler; second order explicit method
Heun's method	Comparable to CK-4	3rd; distant to AB-2	2nd most space on real axis; most space on imaginary axis	Second order predictor-corrector
Fourth order Crane-Klopfenstein	Best, especially for higher frequency modes	4th; distant to Heun's method	Most space on real axis; least space on imaginary axis	Fourth-order predictor-corrector

3.5 Time-Domain Simulation Results with High PV Penetration

Previously, we utilized PST's linearization capabilities to estimate system eigenvalues and identify various modes present in example power systems. In order to measure the prevalence of each mode, particularly the interarea and local modes, we sought to excite each test system and examine its time domain response to various perturbations. This allowed us to corroborate the time domain responses with the system modes as viewed from the frequency domain. By looking at specific time domain responses such as machine speed differences, we were able to identify interarea and local modes and map them to system eigenvalues identified in the stiffness analysis. As in the stiffness analysis, we focused on examining the smaller KRK system and the larger mini-WECC system.

3.5.1 Signal processing architecture

In order to perform mode identification of time domain signals, we developed a specific signal processing architecture. The general structure of our time domain simulations began with a few seconds of steady state to initialize the numerical integrators and proceeded with some type of perturbation to excite system modes, e.g., a three-phase fault or generation drop. In these time domain simulations, we used a fixed step size of a quarter cycle corresponding to a sampling frequency of 240 Hz.

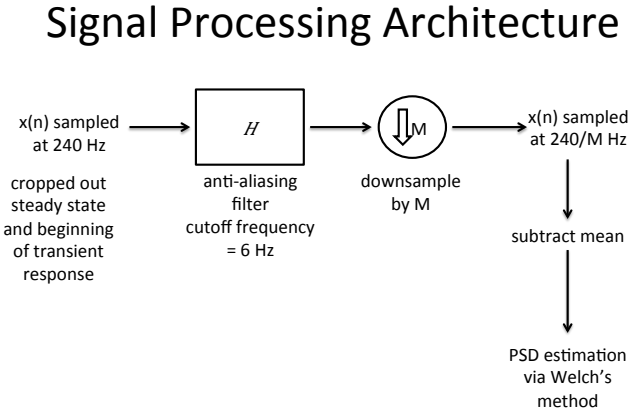

Figure 33: Signal processing architecture summary.

The signal processing architecture developed is summarized in Figure 33. Since we are primarily interested in the system response to a perturbation, we first crop the signal of interest to ignore the steady state and very beginning of the perturbation response. In the case of a three-phase fault simulation, we do this to approximate isolating the impulse response of the system. Since the power system dynamics we are interested in tend to occur in the 6 Hz or slower regime, it is unnecessary to perform a frequency domain transformation on the entire signal. For easier analysis, we implemented a downsampling routine to remove superfluous signal samples. We pass the cropped signal through an anti-aliasing filter whose nominal cutoff frequency is 6 Hz. This anti-aliasing filter is implemented as a third-order Butterworth low pass filter (c.f. Figure 34) which was selected because of its maximally flat passband and smooth

rolloff past the cutoff frequency [18]. Following this filtering, we downsampled the resulting signal by a factor of M which was tuned to comply with the Shannon-Nyquist reconstruction condition in addition an engineering safety factor, γ:

$$M = \frac{1}{\gamma}\frac{1}{2}\frac{f_s}{f_c} \tag{3.24}$$

where $\gamma = 10$, f_s = the sampling frequency, 240 Hz, and f_c = the cutoff frequency, 6 Hz. The resulting signal is effectively sampled at 240/M Hz. Since we are focused on analyzing oscillatory behavior, we subtract the mean of the signal to produce a zero-mean signal.

To preserve spectral features and limit undesirable noise such as spectral leakage from sidelobes attributed to transforming finite duration signals, we applied a signal window to the zero-mean signal before passing it to a power spectral density (PSD) estimation routine. We found that a periodic Blackman windowing signal (c.f. Figure 34) produces the clearest PSD estimates due to its compatibility with discrete Fourier transformations [19]. Finally, we used Welch's method for PSD estimation due to its noise reduction properties [20]. Overall, in comparison to a standard FFT procedure without any additional processing, this signal processing architecture is able to produce much clearer spectral peaks which is a boon for corroborating with the stiffness analysis results.

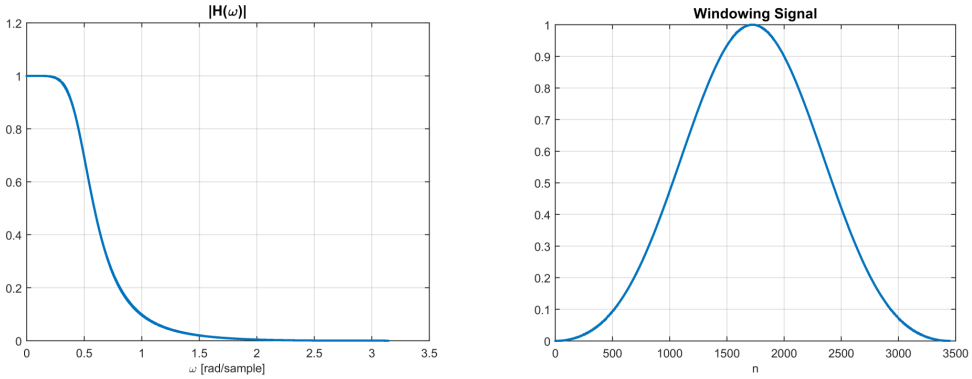

Figure 34: Components of signal processing architecture. (left: anti-aliasing filter frequency response magnitude, right: windowing signal)

3.5.2 KRK system simulations

Three-phase fault with no PV generation For this simulation, we induced a three-phase fault at Bus 3, in area 1 near the central load of the system. This fault was induced after five seconds of steady state and the total simulation time was 40 seconds.

Throughout these examples, we examined the machine speed differences between machine 1 and machine 3, which are in different areas, as well as the machine speed differences between machine 1 and machine 2, which are in the same area. This was done to aid in identifying interarea and local modes, respectively.

Local machine speed difference The local machine speed difference (c.f. Figure 36) doesn't appear to be dominated by a single mode, as evident in the activity of the early response. This indicates there being a non-negligible relatively higher frequency component with a relatively faster rate of decay than the other mode present in the response. This figure displays the estimated power spectral density. It is normalized

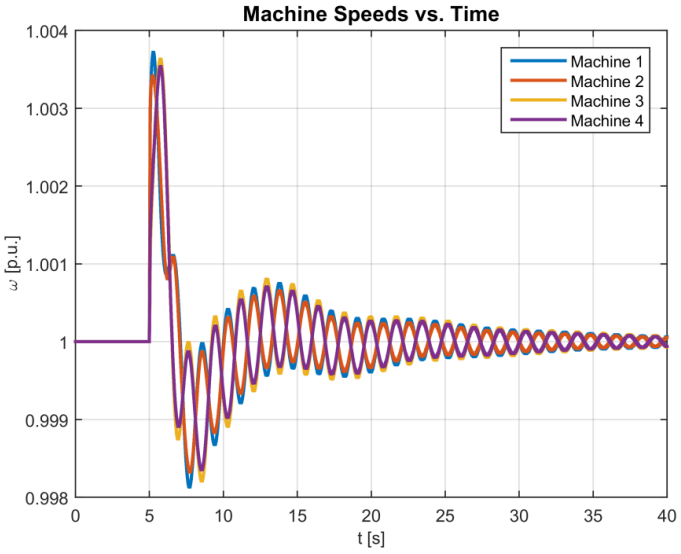

Figure 35: Machine speed responses.

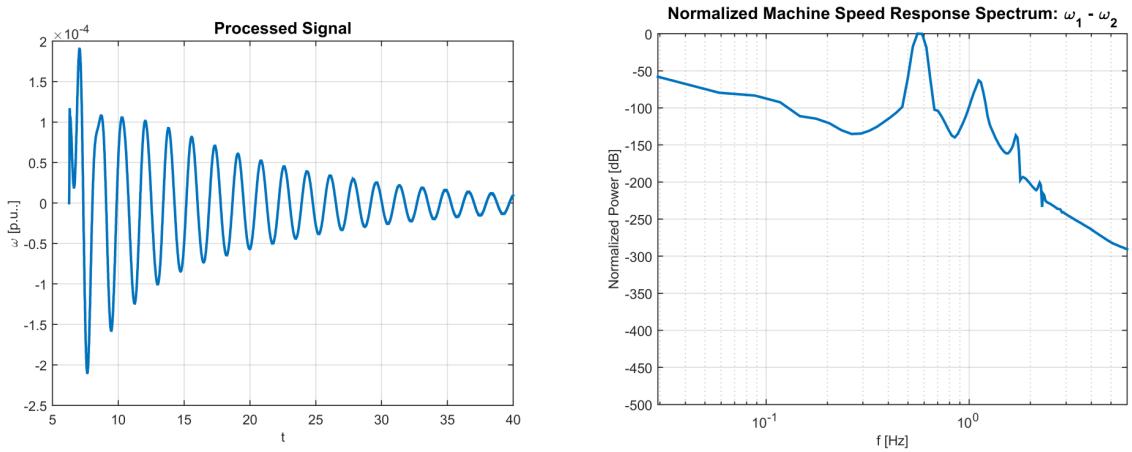

Figure 36: Response signal after processing and corresponding estimated spectrum.

such that the maximum power indicated is 0 dB. The identified peaks in this spectrum are at 0.571 Hz and 1.113 Hz although the latter may simply be a harmonic of 0.571 Hz. These modes can be readily matched to modes identified from the stiffness analysis.

Interarea machine speed difference The response signal in this case appears to be dominated by a single mode evidenced by the smooth decay envelope (c.f. Figure 37). Using a rough estimation method which assumes a single mode, the time constant of the envelope was estimated to be approximately $0.0816s^{-1}$. The estimated PSD identifies the highest energy frequency to be approximately 0.571 Hz. This matches an identified mode at (-0.07928, 0.571) in the (s^{-1}, Hz) plane.

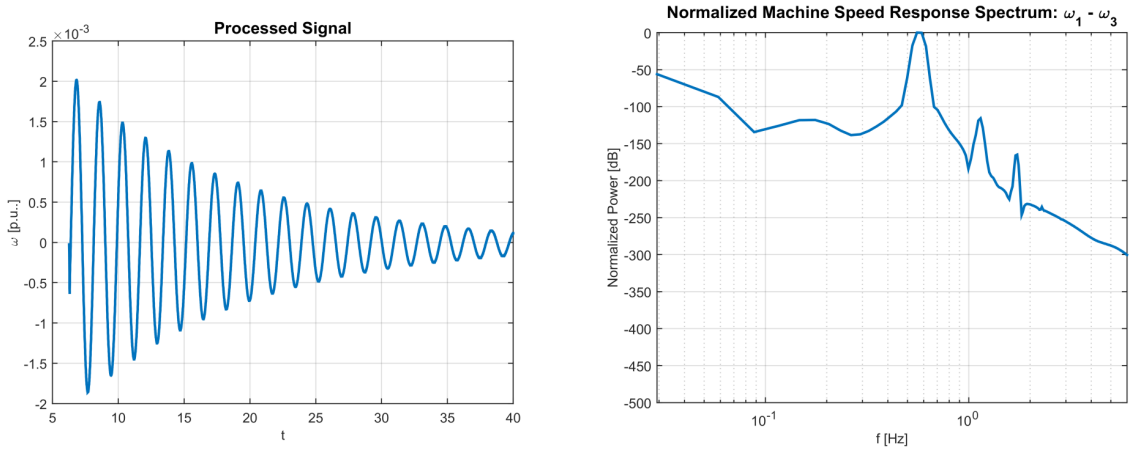

Figure 37: Response signal after processing and corresponding estimated spectrum.

Three-phase fault with 50% PV generation In this example, PV generation was co-located with G2, G3, and G4. Like in previous examples, 50% PV generation indicates that 50% of the active power generated from each synchronous/PV generation pair comes from PV and the rest comes from the synchronous machine; additionally, the synchronous machine has 50% of its original MVA base and, consequently, 50% of its original inertia.

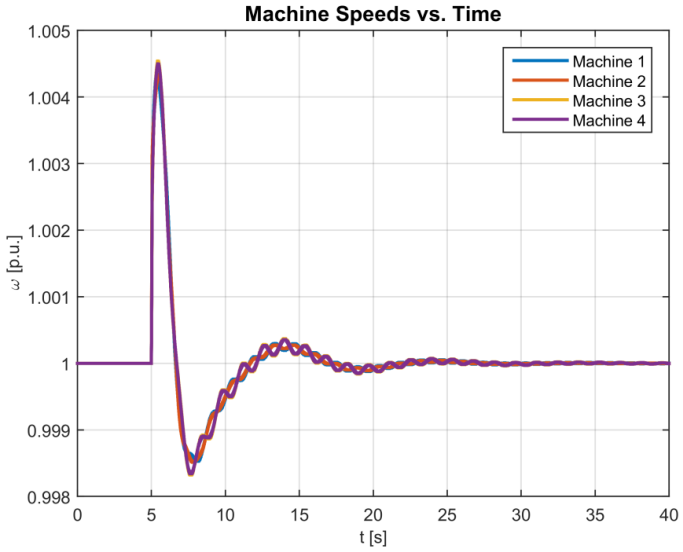

Figure 38: Machine speed responses.

Local machine speed difference In this example, we can observe significant contributions from other mode(s) at the beginning of the disturbance response. The identified peaks in the spectrum are at 0.703 Hz and 1.201 Hz with the latter not being attributable to being a harmonic. The former peak can be matched to an identified mode at ($-0.09358s^{-1}$, 0.7044 Hz). The other peak can be matched to an identified mode

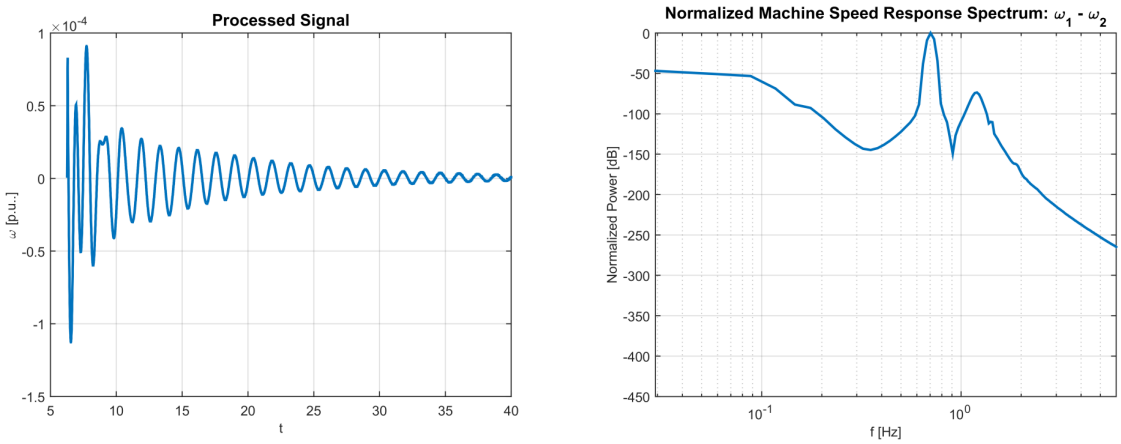

Figure 39: Response signal after processing and corresponding estimated spectrum.

at $(-0.785s^{-1}, 1.194$ Hz]. By examining the mode shape of this particular mode (c.f. Figure 40), we can verify that this identified peak is indeed a local mode.

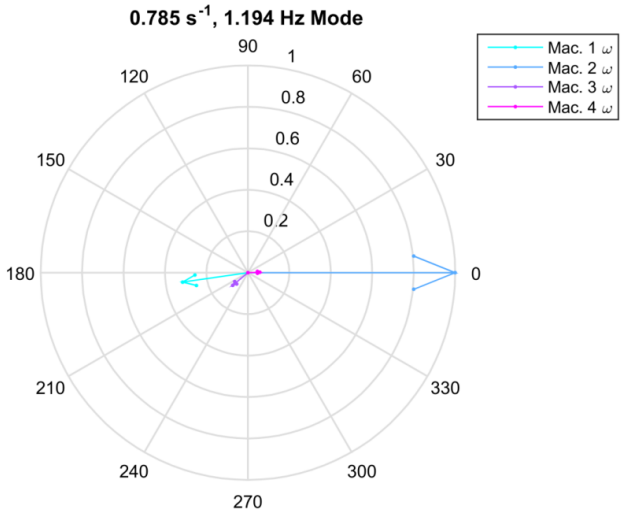

Figure 40: Compass plot illustrating mode shape of the identified local mode.

Interarea machine speed difference There appears to be some more transient activity towards the beginning of the response but it otherwise appears to be dominated by a single mode. Using the aforementioned estimation technique, the time constant of the decay envelope was estimated to be approximately $0.0942s^{-1}$. The identified peak from the estimated spectrum is at 0.703 Hz; this matches the mode to the estimated system eigenvalue at $(-0.09358s^{-1}$, 0.7044 Hz) which we can readily label as the interarea mode based on our previous examples.

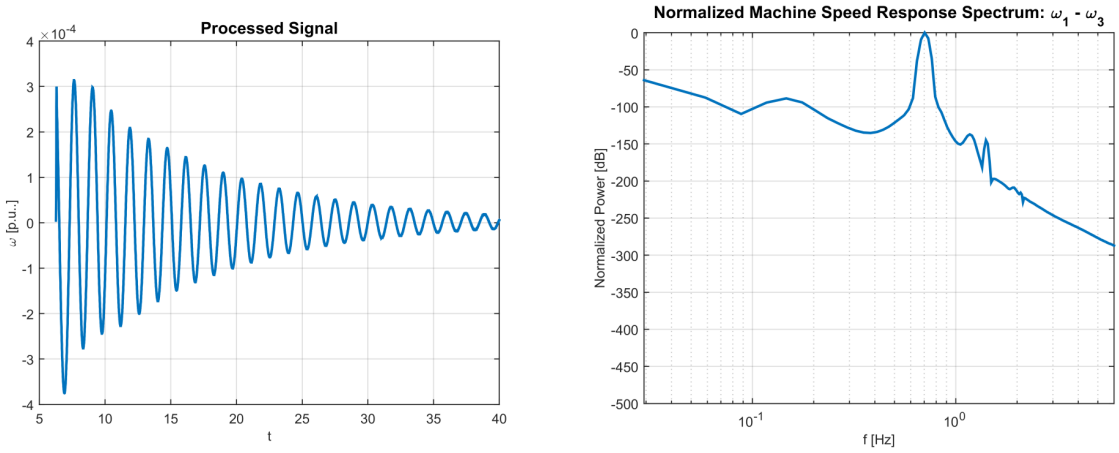

Figure 41: Response signal after processing and corresponding estimated spectrum.

Active power generation drop One transient event of interest to simulate is the sudden increase or decrease in power output of a generator, sometimes called a "generation drop." This is representative of the outage of a single generator among an aggregate collection at a single location. In order to simulate this type of event, we split the active power generation of a representative generator between two identical machines sharing the same point of interconnection to the rest of the system. To simulate the drop in generation, a loss of line (with no fault) event was induced at a particular time, causing a fraction of active power generation at particular location to be disconnected from the rest of the system.

Modifying the KRK system, we included PV generation at G2 and G4. At G3, we split the total active power generation into two identical machines with an 80%/20% split between the two; the total inertia of the pair was split into the same proportions. Both machines were connected to bus 110 with identical lines. To simulate the generation drop, the loss of line event was induced at the line connecting the 20% share machine to bus 110.

We sought to examine the effect of PV penetration levels on the system's responses to this type of event. The response signal of interest was the average machine speed as a function of time. Key features of the response curves include the frequency nadir as well as the steady state settling frequency. The responses are shown in Figure 42.

In order to examine the relative trends of the response curve features, we applied a moving average filter to each response signal in order to smooth out high frequency content. While this had an apparent effect on the nadir frequency, it did not change the relation among the different response signals. The resulting signals are shown in Figure 43.

The response curve characteristics are summarized in the table below. In general, increasing PV penetration delayed the nadir and decreased its frequency and also decreased the steady state frequency. These effects can be attributed to the reduction of inertia in the system.

3.5.3 miniWECC system simulations

As in the KRK system simulations, we sought to verify that the modes estimated through PST's linearization routine would be present in transient event response simulations for the miniWECC case. To do so, we simulated three-phase faults and analyzed machine speed difference signals using our signal processing

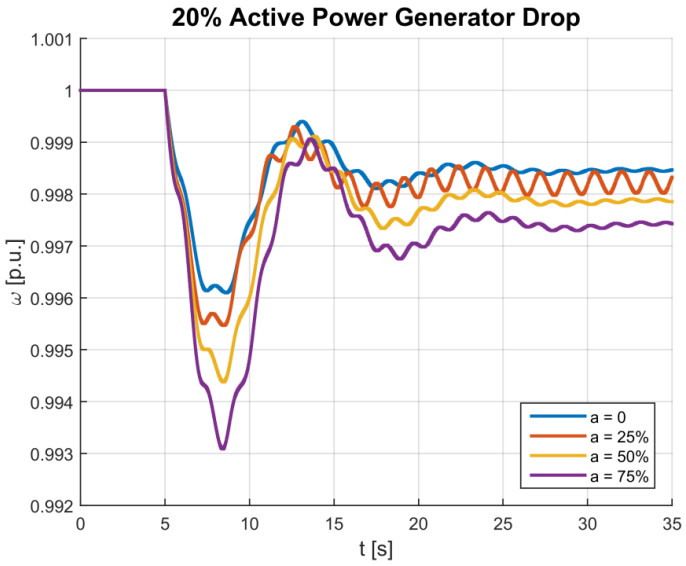

Figure 42: Unfiltered mean machine speed over the four machines in the system.

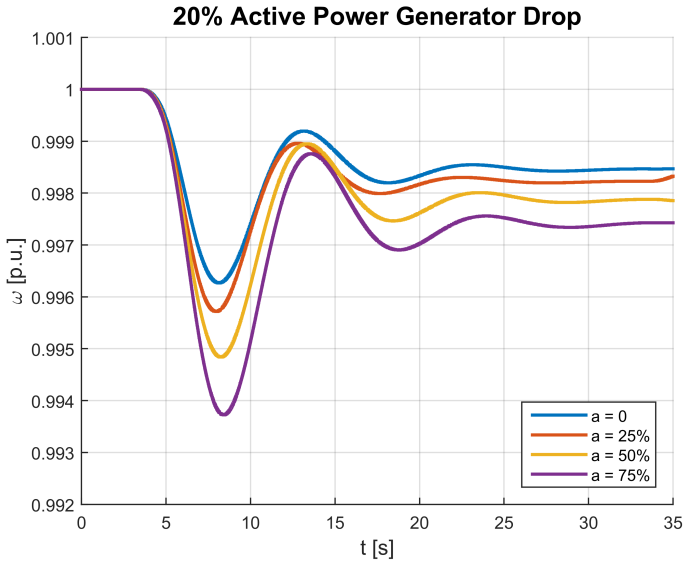

Figure 43: Filtered mean machine speed over the four machines in the system.

architecture to estimate the spectra of the responses. Relevant machines were selected based on the mode shapes that we identified during the stiffness analysis. For example, for North-South Mode A, the Alberta and Arizona machine speeds were the most out of phase out of all machine speeds based on the estimated mode shape. Therefore, in order to try to identify North-South Mode A through these fault simulations, we used the machine speed difference between Alberta and Arizona as the signal for processing.

Table 8: KRK generation drop machine speed response summary.

PV%	Nadir Time [s]	Nadir Speed [p.u.]	Steady State Speed [p.u.]
0%	10.06	0.9966	0.9985
25%	10.07	0.9961	0.9982
50%	10.29	0.9952	0.9979
75%	10.36	0.9942	0.9974

North-South Mode A As mentioned, North-South Mode A was identified using the machine speed difference signal between Alberta and Arizona. In Figure 44, the resulting estimated spectra for the base case and the case with 50% PV are shown. Compared to the KRK system analysis, the spectra for these responses tend to have more identifiable peaks in frequency. For the base case, the dominant frequency was found to be 0.2197 Hz and for the 50% PV case, it was found to be 0.3076 Hz. From the stiffness analysis, these were estimated to be 0.219 Hz and 0.302 Hz, respectively. Slight differences in identified mode frequencies could be attributed to the inherent tradeoff of using Welch's method for power spectral density estimation; noise reduction is gained at the cost of frequency resolution when using the method.

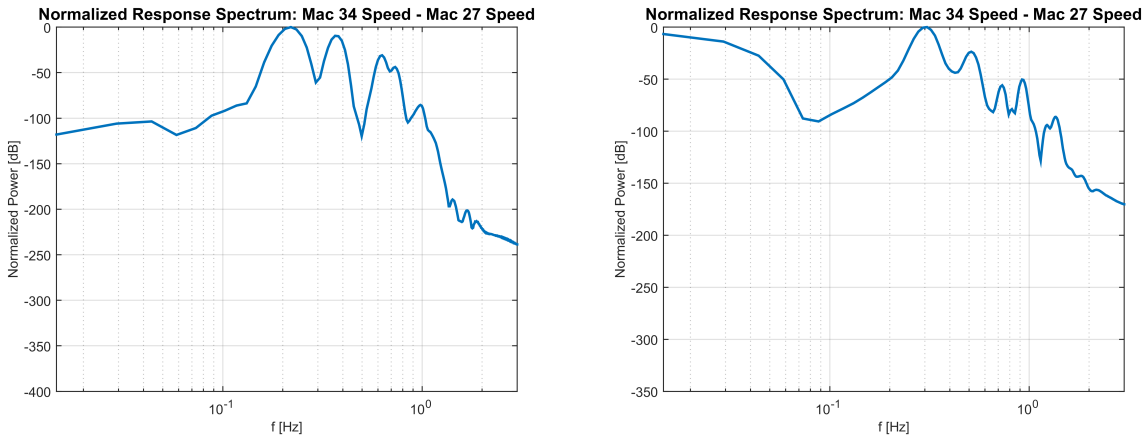

Figure 44: Estimated spectra for identifying North-South Mode A. (left: base case, right: 50% PV)

North-South Mode B To identify North-South Mode B, we looked at the machine speed difference between Alberta and BC. In Figure 45, we compare the spectra from the base case and the 50% PV case. For the base case, the dominant frequency was found to be 0.3662 Hz while for the 50% PV case, it was found to be 0.5127 Hz. These frequencies were estimated to be 0.372 Hz and 0.517 Hz, respectively, from the linearization process. Once again, we found that the frequencies determined through both processes agree closely.

Palo Verde drop simulations One of the common events that are simulated for the system described by the miniWECC case is known as the "Palo Verde drop." One of the buses in the miniWECC case represents the Palo Verde Nuclear Generating Station, the largest power plant in the United States in terms of net generation, which is located in Arizona. It consists of three reactors which, aggregated, provide 12.3 p.u.

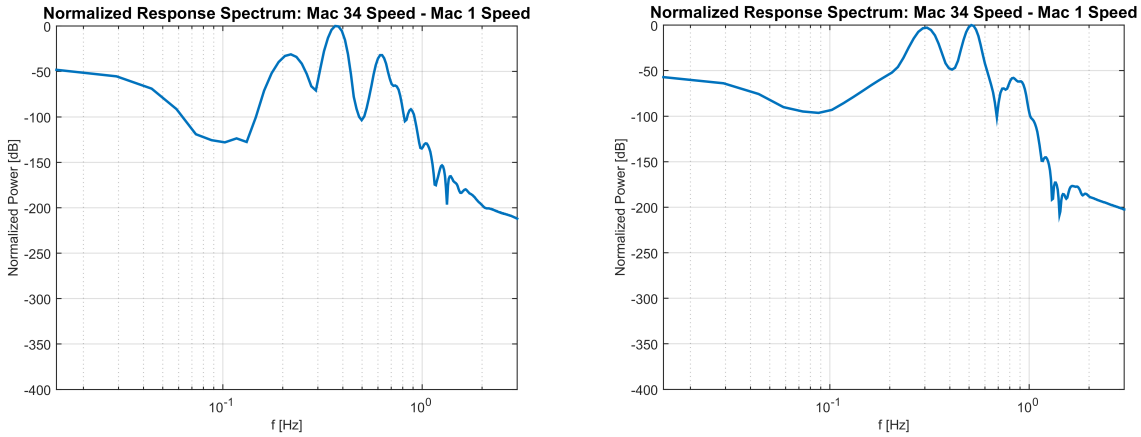

Figure 45: Estimated spectra for identifying North-South Mode B. (left: base case, right: 50% PV)

active power on a 100 MVA base each in the miniWECC system. In the Palo Verde drop simulations, we simulate the loss of one or two of these reactors, similarly to the active power generation drop simulations in the KRK system. Likewise, we use the mean machine response to analyze how increased PV penetration affects the entire system's behavior in response to these events. As in the previous generation drop simulations, increased PV% results in deeper nadirs, slower settling times, and lower steady state machine speeds, all of which are behavior characteristic of reductions in inertia. Furthermore, these behaviors are exacerbated when more generation is dropped, e.g., double Palo Verde drop compared to single drop.

Summary The objective of these time domain simulations was twofold. We sought to validate the results of Section 3.3 by corroborating the modes estimated through eigenanalysis with those that could be excited through small perturbations of the system. We also sought to analyze dynamic behavior of systems in response to disturbances and how this behavior would be affected by increased photovoltaic penetration. We were able to accurately match modes estimated in Section 3.3 by simulating three-phase faults and applying our signal processing architecture to estimate the power spectral density of the resulting responses. Although we already determined that system stiffness is not a sufficient indicator of the requirements for numerically simulating a power system, we demonstrated that it is important to consider external factors such as unit decommitment when increasing PV penetration when performing simulations; such factors may affect, for example, the range of dynamics that need to be simulated (e.g., by removing the fastest modes) and/or change system response behavior entirely (e.g., the disappearance of interarea modes). Trends observed in our simulations include increased decay rates of modes (but not necessarily increased damping) with increased PV penetration as well as deeper machine speed nadirs and lowered steady state machine speeds in generation drop events.

3.6 Loose Ends

In this study, we primarily focused on improving the viability of dynamic simulations as described in the report's title from the perspective of modifying the numerical integration schemes that are used. We've also addressed the path of considering variable time step integration methods which are sparingly used today.

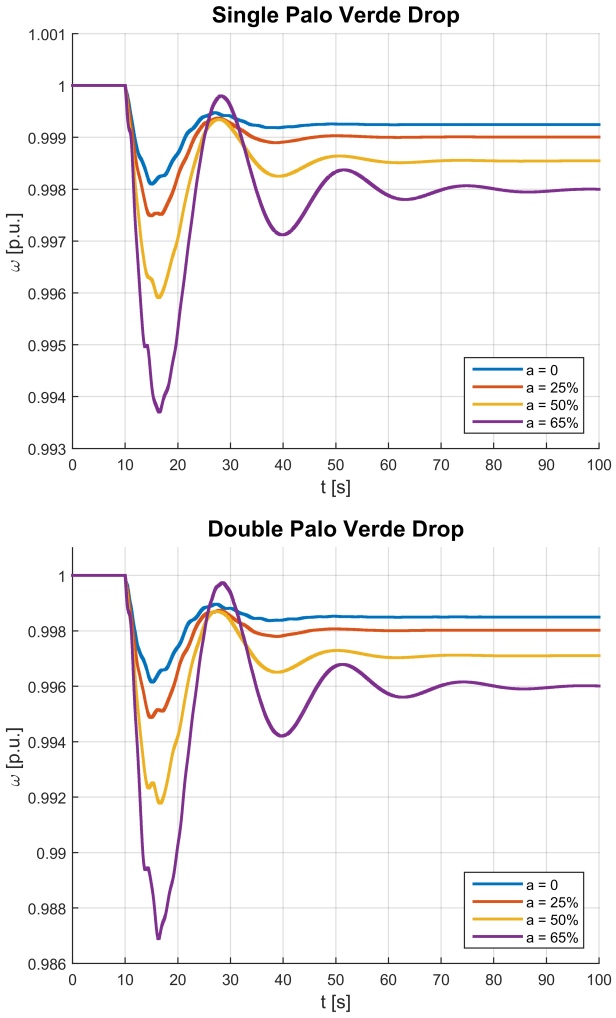

Figure 46: Mean machine speed response to Palo Verde drops.

3.6.1 Slow dynamics modeling

The basic modeling/simulation framework for power system studies has evolved over several decades according to the needs of power system planners and operations staff. The existing framework involves modeling and simulation in three distinct timeframes: steady-state models and studies to investigate system loading conditions and voltage profiles; "transient stability" models and simulation tools to investigate primarily the electro-mechanical interactions of classic rotating generators with one another; and "electro-magnetic transient" models and simulation tools to investigate high-speed phenomena such as lightning strikes. For each of these three timeframes, power engineers have devised models and mathematical solution techniques appropriate to the problem.

PV generating stations do not fit well into classical "transient stability" study paradigm. PV sources are inverter-coupled, and so they do not exhibit the electro-mechanical properties of classic rotating generators. Furthermore, PV sources are generally intermittent and therefore they pose new and previously understudied issues to the power engineering community. For example, the timeframes associated with PV

intermittency is very difficult to model with classical transient stability simulation tools. Those tools are not well equipped to incorporate AGC action or dynamic redispatch algorithms.

There is a need to modify our existing suite of power system simulation tools to incorporate longer term control action such as AGC or dispatching on 5-minute schedules. Two approaches are examined: variable time step simulations and adaptive modeling. The two approaches are complimentary, i.e. it is prudent and appropriate to increase the simulation time step when models incorporating fast dynamics are "swapped out" of a simulation.

This work promises to greatly enhance the capabilities of simulation high penetration PV scenarios by improving our ability to model and simulate longer-term dynamics. The primary issues associated with high penetration scenarios may not lie with electro-mechanical interactions, but may instead lie with our ability to effectively redispatch generation dyanamically. The new simulation framework offers to provide the engineering community with the tools to study these effects.

In addition to these modeling needs, other effects need to be considered, including prime mover effects, state of charge tracking for energy storage systems, wind speed variations, and solar irradiance variations. These dynamics, which play out over time frames of several minutes, are typically neglected due to most simulations being limited to about 60 seconds in duration.

3.6.2 Stakeholder feedback

We presented our analysis at various WECC Renewable Energy Modeling Task Force (REMTF) meetings over the course of the project and received feedback from stakeholders and vendors. In addition to the slow system dynamics modeling gaps addressed, attention was also given to the fast system dynamics that are typically not modeled in positive sequence modeling environments. Such dynamics include those of the phase locked loop (PLL) systems used for frequency and phase detection and the inner current regulators, both of which have dynamics well into the kilohertz range.

One idea for improving feasibility of extended term simulations included throwing out faster dynamics to enable the opportunity to, e.g., increase simulation step size. While it is plausible that the effects of such faster dynamics may be negligible for extended term simulations, it does not seem to be a viable solution if we wish to preserve simulation fidelity as much as possible. One other aspect of system modeling that should be considered is to investigate how interconnection impedance for PV power plants is affected as PV penetration level increases. Increased PV penetration levels would cause low short-circuit ratios, a measure of AC system strength, to become a factor. Wind and solar power plants connected to weak grids with low short-circuit ratios are not uncommon and dynamic models developed by the WECC REMTF are not intended for these plants. This issue ties into the common theme of a current gap in modeling capabilities.

Based on feedback from some software vendors, it was discovered that a significant selection of the dynamic models that have been written in some of the dynamic simulation software used today were written in a way that tie them to the second order Adams-Bashforth integration scheme. As a result, it would require a significant overhaul to change these models to be compatible with other integration schemes, such as those analyzed in this study. While this is a valid concern for current software, we still posit that the development of future simulation software and/or updates to current software should have dynamic models retain the flexibility to be used with any desired integration scheme. This would enable future updates to the software's integrator that could, for example, improve the feasibility of extended-term simulations.

4 Significant Accomplishments and Conclusions

In this one year effort, we examined several of the paths forward that could help dynamic simulation software perform extended-term simulations of power systems with high penetrations of PV generation. Our primary focus was to look at how we could change the way current simulation software performs numerical integration in order to accommodate the needs of high PV penetration systems while managing data and computation concerns that arise with extended simulation durations. We used Power Systems Toolbox (PST) in MATLAB as our research and development platform because of the ability to modify its code as needed. We used a current injection model to represent PV power plants and scaled back the inertia of traditional synchronous machines as generation was shifted to the PV power plants.

We used PST's linearization methods to estimate the eigenvalues of several power system test cases. This allowed us to get an idea of the typical layouts of power systems' eigenvalues and determine the numerical integrator's needs from a numerical stability perspective. This drove us to analyze a set of explicit integration schemes, including Heun's method, the second order Adams-Bashforth method, and the fourth order Crane-Klopfenstein method. We evaluated each of these schemes on their computational performance, accuracy performance, and numerical stability. While we decided that CK-4 had the greatest potential for reducing computational burdens while retaining numerical stability for many simulation scenarios, we also showed that Heun's method had the greatest flexibility while possessing the opportunity to increase simulation step sizes because of its relatively large region of absolute stability. In the event that the system to be simulated does not have fast, high frequency modes, CK-4 is most likely able to increase its step size compared to the other integrators that we evaluated.

While the bulk of our analysis focused on analyzing fixed time step, explicit integration schemes, we also considered the possibility of variable time step integration. Such methods also have potential to improve extended term simulation viability due to their ability to adapt the time step as the system dynamics evolve but require finesse and additional logic (error/time step control) to implement.

When considering extended term simulations, especially in the case of high PV penetration systems, we determined that there are various deficits in power system modeling. Dynamics in both the slow and very fast regimes are not modeled in transient and small signal stabilities due to the scope of the systems typically studied as well as the simulation durations that are typically used. Simulations with minute-long durations do not need to consider phenomena that occur over minutes or hours. Dynamics that are in the kilohertz frequency range are typically negligible in most systems that are simulated. However, all of these dynamics need to be considered when extending the simulation durations and when including large amounts of inertialess PV generation, which behaves significantly differently from conventional synchronous machines.

5 Inventions, Patents, Publications, and Other Results

A conference paper was submitted to the IEEE Power & Energy Society General Meeting 2016. The citation information is listed below:

R. Concepcion, R. Elliott, M. Donnelly, J. Sanchez-Gasca, *On Extended-Term Dynamic Simulations with High Penetrations of Photovoltaic Generation*, submitted to IEEE Power & Energy Society General Meeting, July 2016.

An additional, companion paper was written but is pending submission. The citation information is

listed below:

J. Sanchez-Gasca, R. Concepcion, R. Elliott, M. Donnelly, *Root Locus Analysis of the Generic WECC Photovoltaic Power Plant Model*

A lengthier, more comprehensive SAND report covering the research done for this project will be released as well.

6 Path Forward

In this report, only two test systems were analyzed, the KRK system and the miniWECC. Through past efforts and efforts in this project such as the stiffness analysis and time domain simulations, the qualitative and quantitative results obtained in studies of these systems have been thoroughly validated. As noted in the example of the KRK system in PSLF, discrepancies in system behavior arise from different representations of the system under study. In the case of the KRK system, there is no real system to validate against. For the miniWECC, the base case has been validated through past efforts as cited. However, since the increased PV penetration scenarios studied in this project are purely hypothetical at this point, it is difficult to say how reliable the results produced are, especially due to the relatively simple way that PV was modeled. Therefore, while the conclusions drawn from the studies conducted in this report aimed to be general and be supplemented with the appropriate caveats, future studies on this subject should be cognizant of the immense role that the way that the system is dynamically represented plays.

In conclusion, there are many paths forward to help develop the capability of simulating systems with high PV penetration levels over long time periods. There is room for developing the numerical integration schemes that are used in order to reduce computational and data storage burdens. In this one year effort, we focused on fixed time step, explicit integration schemes. There remains the option of variable time step integration as well as the challenge of overhauling existing integration engines in today's software or developing new platforms that can utilize new integration schemes. There are also gaps in power system modeling capabilities that need to be filled, especially for high PV penetration scenarios. In addition to the slow dynamics such as AGC, others need to be considered, including prime mover effects, state of charge tracking for energy storage systems, wind speed variations, and solar irradiance variations. These dynamics, which play out over time frames of several minutes, are typically neglected due to most simulations being limited to about 60 seconds in duration. Developments in both these regards should pave the way for more realistic simulations of systems with high PV penetration over extended durations.

References

[1] C. Fu, J. McCalley, and J. Tong, "A numerical solver design for extended-term time-domain simulation," *IEEE Transactions on Power Systems*, 2013.

[2] C. Fu, "High-speed extended-term time-domain simulation for online cascading analysis of power systems," tech. rep., Iowa State University, 2011.

[3] B. Ehle, "High order a-stable methods for the numerical solution of systems of d.e.'s," tech. rep., University of Waterloo, 1968.

[4] W. Humpage and B. Stott, "Predictor-corrector methods of numerical integration in digital-computer analyses of power-system transient stability," *Institution of Electrical Engineers Proceedings*, vol. 112, 1965.

[5] M. Y. Borodulin, "Effect of numerical integration on critical time evaluation in power system stability studies," *IEEE Power and Energy Society General Meeting*, 2013.

[6] G. Wanner, "Dahlquist's classical papers on stability theory," *BIT Numerical Mathematics*, vol. 46, 2006.

[7] J. Sanchez-Gasca, R. D'Aquila, W. Price, and J. Paserba, "Variable time step, implicit integration for extended-term power system dynamic simulation," *Power Industry Computer Application Conference*, 1995.

[8] B. Stott, "Power system dynamic response calculations," *Proceedings of the IEEE*, 1979.

[9] R. Elliott, P. Pourbeik, and J. Sanchez-Gasca, "Generic photovoltaic system models for wecc," *IEEE Power and Energy Society General Meeting*, 2015.

[10] J. H. Chow and K. W. Cheung, "A toolbox for power system dynamics and control engineering education and research," *IEEE Transactions on Power Systems*, vol. 7, pp. 1559–1564, November 1992.

[11] D. Trudnowski, D. Kosterev, and J. Undrill, "Pdci damping control analysis for the western north american power system," *Proceedings of the IEEE Power and Energy Society General Meeting*, 2013.

[12] M. Klein, G. J. Rogers, and P. Kundur, "A fundamental study of inter-area oscillations in power systems," *IEEE Transacations on Power Systems*, vol. 6, 1991.

[13] D. Trudnowski, "Properties of the dominant inter-area modes in the wecc interconnect." https://www.wecc.biz/Reliability/WECCmodesPaper130113Trudnowski.pdf, January 2012.

[14] E. H. Abed, D. Lindsay, and W. A. Hashlamoun, "On participation factors for linear systems," *Automatica*, vol. 36, no. 10, 2000.

[15] S. Ranganath and R. J. Clifton, "A second-order accurate difference method for systems of hyperbolic partial differential equations," *Computer Methods in Applied Mechanics and Engineering*, 1972.

[16] R. L. Crane and R. W. Klopfenstein, "A predictor-corrector algorithm with an increased range of absolute stability," *J. ACM*, vol. 12, pp. 227–241, April 1965.

[17] O. Nevanlinna and A. Sipila, "A nonexistence theorem for explicit a-stable methods," *Mathematics of Computation*, vol. 28, 1974.

[18] S. Butterworth, "On the theory of filter amplifiers," *Wireless Engineer*, vol. 7, no. 6, 1930.

[19] A. Nuttall, "Some windows with very good sidelobe behavior," *IEEE Transactions on Acoustics, Speech and Signal Processing*, vol. 29, February 1981.

[20] P. D. Welch, "The use of fast fourier transform for the estimation of power spectra: A method based on time averaging over short, modified periodograms," *IEEE Transactions on Audio and Electroacoustics*, vol. AU-15, June 1967.